

NITROGEN ION BOMBARDMENT OF FUEL CLADDING MATERIALS

A Thesis

by

ELIZABETH DIANE CASTANON

Submitted to the Office of Graduate and Professional Studies of
Texas A&M University
in partial fulfillment of the requirements for the degree of

MASTER OF SCIENCE

Chair of Committee, Lin Shao
Committee Members, Cable Kurwitz
Ankit Srivastava

Head of Department, Yassin Hassan

August 2016

Major Subject: Nuclear Engineering

Copyright 2016 Elizabeth Diane Castanon

ABSTRACT

In a nuclear reactor where there are high stresses, temperatures and radiation levels, a number of material problems can occur including corrosion, thermal fatigue cracking, and embrittlement. Material problems are a serious issue in regards to the performance, the advancement, and the safety of nuclear reactors under accident conditions. Fuel cladding materials are of particular significance since cladding is the most important safety barrier, as it contains the majority of radioactive fission products.

Nitriding is a method proven to improve many material properties including corrosion and wear resistance. Nitriding works by dissolving or implanting nitrogen into the surface of a material where the nitrogen bonds with the material atoms to form nitrides. The nitriding in these studies is performed by the use of ion bombardment with 40 KeV nitrogen atoms.

The purpose of this work is to improve understanding of this type of surface modification on fuel cladding materials. The materials used here are iron, 316L stainless steel, zirconium, and zircaloy-4. The focus of these studies was on fluence dependence and temperature stability of nitride layers induced by ion nitriding. Here it was found that by a fluence of $5E17$ N/cm², both pure Fe and SS316L are saturated and that by a fluence of $1E18$ N/cm², both zirconium and zircaloy-4 are saturated. By 300°C in both Fe and SS316L and 600°C in zirconium and zircaloy-4, metastable nitrides have become unstable and nitrogen begins to diffuse out. Hardness test show that with a combination of irradiation and annealing, each material's hardness can greatly be improved. However, the

high mobility of nitrogen in iron at temperatures above 300°C limits the uses of iron alloys in very high temperature environments like reactors. Zirconium is shown to be stable up to temperatures approximately twice as high as iron indicating nitrides in zirconium alloys maybe able withstand reactor temperatures.

DEDICATION

This thesis is dedicated to my parents who have offered me endless love and support throughout my college education, and my co-workers who have always been there to for help and advice.

ACKNOWLEDGEMENTS

I would first like to thank my committee chair and advisor, Dr. Lin Shao, for accepting me into his research group and giving me guidance throughout the course of my research.

I would like to thank Dr. Lloyd Price. He has been a mentor to me since I joined this research group. He has taught me a great deal of what I now know about accelerators systems, vacuum systems, machining and other lab related areas. He has been dependable for help in my research and in my courses. Lloyd has been a great teacher as well as a great friend.

Jonathan Gigax has also been a wonderful mentor in my time at Texas A&M. He has also taught me a great deal and has challenged me to think harder and do better at everything I work on. He has always been there for help and advice.

Xuemei Wang is the lab manager and constantly pushes me to develop a better understanding of the accelerator equipment. Without her questioning me, there is a lot less I would learn.

I want to thank Tianyi Chen. He took the time to prepare my sample with FIB and also characterize it with TEM.

I would next like to thank Jiangyuan Fan for the long hours he spent electropolishing my samples. Without his help, the surface quality of my samples would have been in danger.

I also want to thank Robert Balerio for doing the hardness testing on my samples. He was willing to work long hours on short notice to help me get the data. His help was crucial in finishing my thesis.

I want to give a special thanks to my friend and colleague Hyosim Kim. She entered the program at the same time as me and shared in all the struggles with research and coursework. Her support helped get me where I am today.

Finally I want to thank all my other friends and colleagues and faculty who have taught me and made my time at A&M memorable.

NOMENCLATURE

ADS	Accelerator Driven System
BCC	Body-Centered Cubic
BWR	Boiling Water Reactor
DHC	Delayed Hydride Cracking
DI	De-Ionized
LWR	Light Water Reactor
PPM	Parts Per Million
PWR	Pressurized Water Reactor
RBS	Rutherford Backscattering Spectrometry
RCIC	Reactor Core Isolation Cooling
SEM	Scanning Electron Microscopy
SNICS	Source of Negative Ions by Cesium Sputtering
SRIM	Stopping Range of Ions in Matter
SS316L	Stainless Steel 316L
TEM	Transmission Electron Microscopy

TABLE OF CONTENTS

	Page
ABSTRACT.....	ii
DEDICATION.....	iv
ACKNOWLEDGEMENTS.....	v
NOMENCLATURE.....	vii
TABLE OF CONTENTS.....	viii
LIST OF FIGURES.....	x
1. INTRODUCTION TO NITRIDING	1
1.1 Benefits.....	3
1.2 A Brief History of Nitriding.....	4
1.3 Nitriding Methods	5
1.4 Previous Works	11
2. NUCLEAR MATERIAL PROBLEMS	13
2.1 Fuel Cladding Materials	13
2.2 Thermal Fatigue Cracking.....	16
2.3 Wear	18
2.4 Delayed Hydride Cracking.....	19
2.5 Corrosion.....	21
2.6 Fukushima Daiichi Explosions.....	22
3. RUTHERFORD BACKSCATTERING ANALYSIS	25
3.1 Geiger - Marsden Experiments.....	26
3.2 Theory	29
3.3 RUMP.....	37
3.4 Equipment	39
4. EXPERIMENT DESIGN.....	41
4.1 Materials.....	41
4.2 Sample Preparation.....	42

4.3 Irradiation and Annealing.....	43
4.4 Equipment	44
4.5 Data Acquisition.....	46
5. IRON AND SS316L.....	47
5.1 Dose Dependence Results	47
5.2 Temperature Stability Results	50
5.3 Characterization of Nitrides in Saturated Iron	54
5.4 Conclusions	57
6. ZIRCONIUM AND ZIRCALOY-4	62
6.1 Dose Dependence Results	62
6.2 Temperature Stability Results	64
6.3 Conclusions	67
7. SUMMARY	72
REFERENCES.....	74
APPENDIX A	78

LIST OF FIGURES

	Page
Figure 1.1: Simplified image of ion nitriding process.	2
Figure 1.2: Diagram of the nitride layer typically formed during the nitriding process. ...	6
Figure 1.3: Image of glow discharge from plasma nitriding of gears.	8
Figure 1.4: Post corrosion SEM micrograph of (a) as received steel and (b) plasma nitrided steel [9].	11
Figure 1.5: Optical profilometry of the wear tract for H13 samples at 600°C A) uncoated and B) with a gas nitrided layer [10].	12
Figure 2.1: A nuclear fuel assembly with the rod cluster control assembly [12].	14
Figure 2.2: Fuel rod with depiction of pellet and cladding placement [14].	15
Figure 2.3: 316L steel specimen after undergoing thermal fatigue testing [17].	17
Figure 2.4: Picture of the grid-to-rod assembly [19].	18
Figure 2.5: Picture of a hydride area and crack [24].	20
Figure 3.1: Diagram of He ion collisions in RBS.	26
Figure 3.2: Schematic of Rutherford's gold foil experiment.	28
Figure 3.3: Diagram of the RBS setup used in experiments.	29
Figure 3.4: RBS sensitivity for various elements using a 2 MeV He beam.	32
Figure 3.5: Simulated RBS spectrum of a WSi layer on a Si substrate.	35
Figure 3.6: Picture of typical user interface with RUMP software.	38
Figure 3.7: Simplified diagram of 1.7 MV tandem accelerator used for RBS.	40
Figure 4.1: Simplified diagram of the 140 KV particle accelerator.	45

Figure 5.1: RBS spectra and associated nitrogen profiles of pure iron irradiated to A) 1E17 N/cm ² , B) 5E17 N/cm ² , C) 1E18 N/cm ² , D) 2E18 N/cm ² and E) the concentrations plotted for each dose.	48
Figure 5.2: RBS spectra and associated nitrogen profiles SS316L irradiated to A) 1E17 N/cm ² , B) 5E17 N/cm ² , C) 1E18 N/cm ² , D) 2E18 N/cm ² and E) the concentrations plotted for each dose.	49
Figure 5.3: Hardness of iron and SS316L at increasing doses.	50
Figure 5.4: RBS spectrum of saturated iron post annealed at A) room temperature, B) 100°C, C) 300°C, and D) 500°C.	51
Figure 5.5: RBS spectrum of saturated SS316L post annealed at A) room temperature, B) 100°C, C) 150°C, and D) 300°C.	52
Figure 5.6: Hardness of iron and SS316L at increasing temperatures.	53
Figure 5.7: TEM micrographs of (a) a cross sectional view of 5×10 ¹⁷ N-implanted Fe at room temperature with “Area 1” referring to N implanted region and “Area 2” referring to un-implanted region, (b) the diffraction pattern of area 2, (c) a HRTEM obtained from area 2 at the [111] matrix zone axis, (d) the FFT pattern of (c), (e) a HRTEM obtained from area 1 at the [331] matrix zone axis, (f) the inversed FFT pattern of (e), and (g) the indexed FFT pattern of (e) with the circles referring to the diffraction spots used to construct (e).	56
Figure 5.8: TEM micrographs of (a) a high resolution cross sectional view of 5×10 ¹⁷ N-implanted Fe at room temperature, obtained from N-implanted region, (b) the corresponding inversed FFT pattern, (c) the corresponding indexed FFT pattern with the circled spots used to construct (b), (d) the schematics of the FeN ₂ crystal structure with blue color referring to N atoms and red color referring to Fe atoms, (e) the comparison of inverse FFT pattern and projected view of the FeN ₂ crystal structure, and (f) simulated diffraction patterns.	57
Figure 5.9: SRIM calculations of ion ranges in A) iron and B) SS316L [37].	58
Figure 5.10: Hardness results based on studies by Fujihana [39].	59
Figure 5.11: Fe-N phase diagram based on findings by du Marchie with augmented γ''-FeN and γ'''-FeN phases [45].	60

Figure 6.1: RBS spectra and associated nitrogen profiles of pure zirconium irradiated to A) $1\text{E}17\text{ N/cm}^2$, B) $5\text{E}17\text{ N/cm}^2$, C) $1\text{E}18\text{ N/cm}^2$, D) $2\text{E}18\text{ N/cm}^2$ and E) the concentrations plotted for each dose.	62
Figure 6.2: RBS spectra and associated nitrogen profiles of zircaloy-4 irradiated to A) $1\text{E}17\text{ N/cm}^2$, B) $5\text{E}17\text{ N/cm}^2$, C) $1\text{E}18\text{ N/cm}^2$, D) $2\text{E}18\text{ N/cm}^2$ and E) the concentrations plotted for each dose.	63
Figure 6.3: Hardness of zirconium and at increasing doses.	64
Figure 6.4: RBS spectrum of saturated zirconium post annealed at A) room temperature, B) 500°C , and C) 600°C	65
Figure 6.5: RBS spectrum of saturated zircaloy-4 post annealed at A) room temperature, B) 500°C , and C) 600°C	66
Figure 6.6: Hardness of saturated zirconium and at increasing temperatures.	67
Figure 6.7: Ion ranges of A) zirconium and B) zircaloy-4 calculated by SRIM [42].	68
Figure 6.8: Nitrogen-zirconium phase diagram [47].	69
Figure 6.9: Oxygen-zirconium phase diagram [47].	70
Figure A.1: Picture of RUMP software opening display.	78
Figure A.2: Picture of directory change input in RUMP.	78
Figure A.3: Picture of data from a typical RBS text file.	79
Figure A.4: Picture of swallow command used in RUMP.	79
Figure A.5: Picture of plot command used in RUMP (left) and associated generated graph of data (right).	80
Figure A.6: Picture of write command used in RUMP.	80
Figure A.7: Picture of input text file for RUMP.	81
Figure A.8: Picture of input text file and associated RUMP plot.	82
Figure A.9: Picture of simulation and data plots generated by RUMP.	82
Figure A.10: Picture of commands used to save data file.	83

1. INTRODUCTION TO NITRIDING

An important step in making advancements in nuclear reactors is developing materials which can withstand harsher environments including higher stresses, temperatures, and radiation. This is especially true in regards to fuel cladding where material improvement affects the efficiency and lifetime of the reactor as well as its safety. There exist many methods to improve material properties including grain size augmentation, cold working, alloying and a variety of surface treatments. However in the case of fuel cladding, it is important to keep the material core properties, like ductility, which eliminates all methods but surface treatments. Still, even with many surface treatment methods, materials may delaminate under reactor operating conditions [1].

Nitriding may be a solution. Nitriding works by dissolving or implanting nitrogen into the material matrix where it bonds with the metal to form nitrides near the surface. Because the nitride is formed inside the original material matrix instead of at the surface, the nitride treatment has a lower potential to delaminate in a reactor. Nitriding has been shown to improve many properties including wear resistance, corrosion resistance and hardness. The process can also be performed under relatively low temperatures and does not require quenching. Thus there is no phase change in the host material and little to no distortion [2].

The purpose of this work is to improve understanding of surface modification by nitriding on fuel cladding materials. The focus is on the fluence dependence and temperature stability of nitride layers induced by ion nitriding.

For the experiments presented here, a type of nitriding known as ion nitriding was utilized. In ion nitriding, nitrogen becomes incorporated into a sample by ion bombardment. The system may become thermodynamically unstable. New phases can form and a nitrogen enriched layer, thicker than the typical implantation depth, results from diffusional transport. In ion bombardment, energetic ions impinge on a sample where they will be reflected or implanted within. They may also displace substrate atoms or remove atoms from the substrate. A simplified image of ion nitriding can be seen in Fig. 1.1 where the nitrogen beam impinges on the sample, and nitrogen begins migrating to interstitial positions. Then as more nitrogen is applied, a layer forms beneath the first layer of interstitial nitrogen and alloying-elements-nitride precipitates.

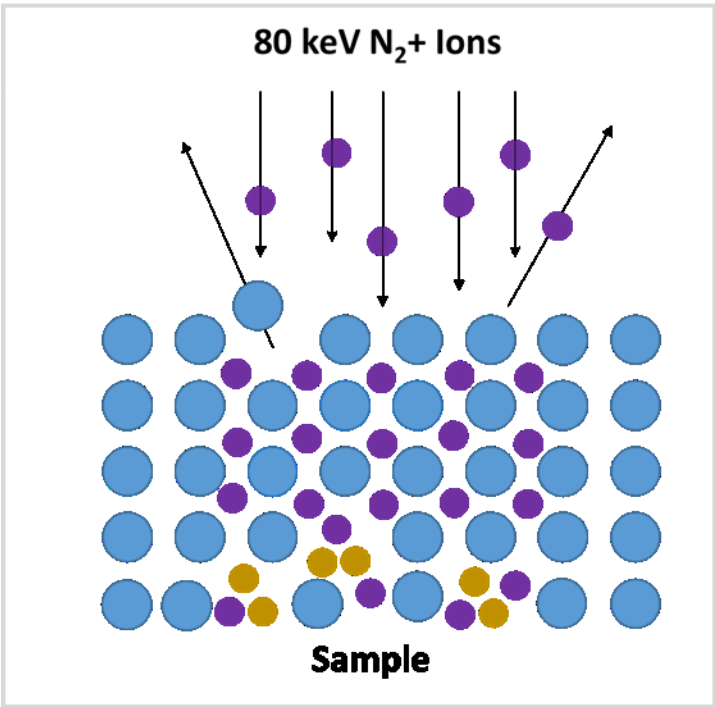


Figure 1.1: Simplified image of ion nitriding process.

Perhaps the most important measure to consider is the nitrogen concentration since it affects almost all the properties of the nitride layer including the thickness and phases formed.

1.1 Benefits

Nitriding is the introduction of nitrogen into the surface layer of a material while holding the material at a low enough temperature that no phase transition takes place [1]. Quenching is also not required to produce a nitride layer. This is a significant advantage over many other surface treatments, like carburizing. In those processes, high temperatures and phase transitions result in substrate softening and distortion. In addition, with nitriding layer thickness can more easily be controlled and consistent treatments can be done [2]. The nitride layer created by the nitriding process greatly enhances surface properties while retaining the core properties of the material. Those properties include hardness, anti-galling, and abrasive, wear and corrosion resistance. This has made nitriding useful in the manufacturing of machinery parts including bearings, automotive components and aircraft components.

The material property enhancements afforded by nitriding, especially wear and corrosion resistance, could greatly improve the integrity of fuel cladding. Improved resistance to failures means the cladding could be used longer in the reactor. One of the limiting factors for how long fuel can be used in the reactor is how long the fuel elements, like cladding, can retain their integrity. Using more advanced reactor materials would allow for better integrity and thus the potential for longer lifetimes and more efficient use

of fuel. Also, the nitride layer is created within the original material matrix increasing the potential to remain intact under nuclear reactor operating conditions where materials are subjected to high stresses, temperatures and radiation. This increased potential is in contrast to other surface treatments such as vapor depositions which create layers on top of the material matrix and have been shown to delaminate in a reactor environment.

Historically, nitriding has been predominately done with iron and iron-alloy materials. However, it can be used on a variety of metals that have the bonding capability to form nitrides. Presently, nitriding is being increasingly applied to more materials including titanium, aluminum and zirconium alloys.

1.2 A Brief History of Nitriding

The nitriding process can be traced back to the early 20th century with the work of the American metallurgical engineer Adolph Machlet. Carburizing was a surface hardening technique used at the time, but suffered due to distortions produced in the workpieces. Since the distortions were mainly due to extended periods at elevated temperatures followed by rapid quenching, Machlet searched for a different method under which relatively low temperatures and longer cool down times could be used. He found that nitrogen was very soluble in iron and produced a harder and more corrosion resistant surface in iron and iron alloys. Machlet's first patent on the nitriding process was applied for in 1908 and approved in 1916. The process worked by decomposing ammonia with thermal energy to liberate nascent nitrogen and used hydrogen as a dilutant to control the amount of nitrogen entering the workpiece.

Although Machlet was the first pioneer for the nitriding process, most people recognize German research Adolph Fry as the ‘father of nitriding’. Around the same time as Machlet, he recognized that nitrogen was soluble in iron at elevated temperatures. He applied for a patent in 1921 and was granted it in 1924. He used a similar method to Machlet except he did not use hydrogen. This is the single-stage gas nitriding process in use today.

In the United States, Machlet’s process was seen to have little value in the commercial industry and was not widely accepted. In Germany however, Fry’s process was used heavily and saw great success throughout Europe in industries such as aircraft, textile, railroad, and automobile. By the late 1920s, Fry’s nitriding had worked its way to British and American industrialist and engineers [2].

For decades after Machlet and Fry’s work, researchers studied the various parameters and effects of gas nitriding. It was later found that nitriding could be extended to non-ferrous metals like titanium, zirconium and aluminum which can also form nitrides.

1.3 Nitriding Methods

After developing gas nitriding, other methods were sought out like salt bath. By 1932, plasma nitriding had been developed although it did not gain acceptance until the 1970s. Today research is still being done on forms of plasma nitriding [2].

One of the reasons nitriding gained popularity is because researchers found the process to be much easier to control than carburizing while still greatly improving wear and corrosion resistance [2, 3]. The enhanced properties result from the compound layer

and underlying diffusion zone, displayed in Fig. 1.2, created near the surface region after nitriding [4]. The compound or white layer is composed of nitrides predominately of the base material. The hardened diffusion zone is composed of an interstitial solid solution of nitrogen dissolved in the ferrite lattice and nitride and/or carbon nitride precipitation with the alloying elements, and it results in considerable enhancement of the fatigue endurance of the material. In this study, ion nitriding was used to create nitride layers, but it is worth noting other methods employed in industry today [5].

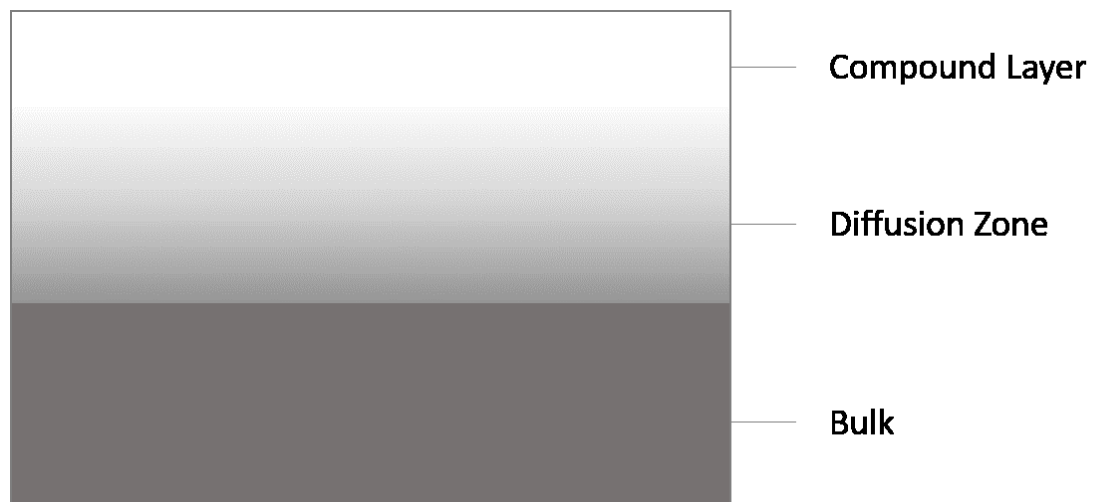


Figure 1.2 Diagram of the nitride layer typically formed during the nitriding process.

The most three important nitriding technologies in use today are salt bath nitriding, gas nitriding and plasma nitriding. Each method has its own benefits and disadvantages, which are summarized in the Table 1. Alternate methods for nitriding are introduced in this section briefly.

1.3.1 Gaseous Nitriding

The gaseous nitriding (GN) process uses gaseous ammonia (NH_3) as a source of nitrogen. When thermal energy is applied to the gas, the ammonia decomposes into its constituents, nitrogen and hydrogen. During cooling, the gas species recombine into ammonia. During nitriding, unstable atomic nitrogen and hydrogen will combine with other atoms to form molecules. The decomposition of ammonia gas is about between 10% and 35% and will vary depending on the steel being treated and the gas exchange rate. The results of the process are evaluated by performing hardness measurements. Gaseous nitriding is one of the most efficient and effective surface methods for improving the surface properties of parts with complicated shapes [5, 6]. Gas nitriding has a current market share of about 75% and is the dominant technology [7].

1.3.2 Salt Bath Nitriding

As the name implies, the salt bath nitriding process is carried out using nitrogen rich salt bath typically including cyanides or cyanates. The process was created as an alternative to gas nitriding because it could produce a more uniform case. The use of the salt bath process is now restricted in many countries due to environmental issues associated with the waste streams produced. In addition, the salt bath process is expensive due to the energy consumption and costs to clean the parts [8]. Thus, salt bath nitriding use is decreasing.

1.3.3 Plasma Nitriding

Conventional direct current plasma nitriding (DCPN) is the most common type of plasma nitriding (PN) available today. DCPN is carried out at in a vacuum chamber with a specified voltage applied between the component to be nitrided and the furnace wall. A glow discharge with a high ionization level (plasma) is generated around the parts as shown in Fig. 1.3. On the surface that is directly charged by ions, nitrogen-rich nitrides are formed and decompose, releasing active nitrogen into the surface. Due to how the nitrogen is introduced into the surface of a part, shielding desired areas from being nitrided is easily done by covering the areas with a metal blanket [9].

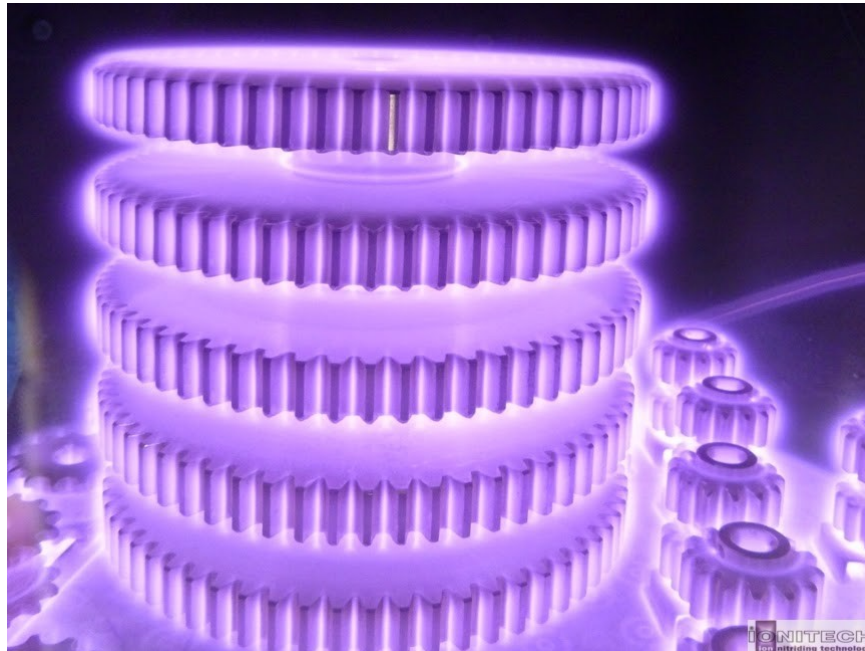


Figure 1.3: Image of glow discharge from plasma nitriding of gears [10].

There are several advantages for PN. First of all, since PN is performed under a high vacuum and a relatively low temperature conditions, there is less distortion compared to gas nitriding. Secondly, after nitriding, the samples will have a higher surface and core hardness than gas nitriding. The increased hardness of the sample results in excellent wear resistance due to the formation of a compound zone that is dense, nonporous, very hard but not brittle, and has a low coefficient of friction. Third, compared to GN, PN is fully automated resulting in more precise control leading to reproducible results. Last, no additional post processing or mechanical treatments are necessary and the need to activate stainless steel is eliminated [11].

Although the DCPN has some remarkable advantages compared to gas nitriding or salt bath nitriding technologies, it also has some limitations related to the formation of the electric field effects. These limitations are listed below:

- Hollow cathode effect: If the parts are placed close proximity or there exists geometries with large length to diameter ratios such as small diameter/deep holes, localized melting will occur due to the sharp discharge gradient. This effect can be minimized by plugging small holes and maintaining adequate space between parts.
- Arcing: The organic degassing in a localized area of a component's surface and the presence of nonmetallic inclusion(s) in the work piece material may produce a very high local temperature which may cause sputtering of the material from localized points on the surface and/or localized melting. Thus, a proper degreasing of the parts is required.

- Edge effect: Sharp corners and/or complex geometries that exist in the components can result in an unevenly nitrated surface and brittleness [12].

Table 1.1: Advantages and disadvantages of nitriding methods [12].

	Advantage	Disadvantage
Salt Bath	<ul style="list-style-type: none"> - Short process cycle - Bulk treatment - Simple handling 	<ul style="list-style-type: none"> - Poisonous waste - High energy consumption - High equipment investment
Gas	<ul style="list-style-type: none"> - Medium term process cycle - Reasonable equipment investment - Process variations possible - Mostly used process of today 	<ul style="list-style-type: none"> - Difficult process control - Low development potential - Needs problematic consumables (ammonia) - Reasonably high energy and gas consumption - Limited in applications
Conventional DC-Plasma	<ul style="list-style-type: none"> - Simple process control - Low energy consumption - No poisonous consumables and waste - High development potential 	<ul style="list-style-type: none"> - High equipment investment - Higher maintenance requirements - Trained staff requested - Limited in applications

Table 1.1 compares the advantages and disadvantages of the three nitriding methods mentioned. Despite the disadvantages of plasma nitriding, its many benefits make it a fast growing field. The hazards of salt bath nitriding however, have resulted in the continual decline of its use. Gas nitriding is able to nitrate complex shapes, but with the new developments being made in active screen plasma nitriding to eliminate electrical effects, even gas nitriding may start to fade in favor of plasma nitriding.

1.4 Previous Works

Extensive studies have been performed on iron alloys demonstrating the potential for nitriding to enhance important material properties. A study by Basu has shown that through plasma nitriding, it is possible to significantly increase the corrosion resistance of steel in terms of corrosion potential, current density and resistance to polarization. Results from the study can be found below in Fig. 1.4. In this study, the nitrided steel was annealed up to 560°C and formed γ' -Fe₄N and ϵ -Fe₂N [13].

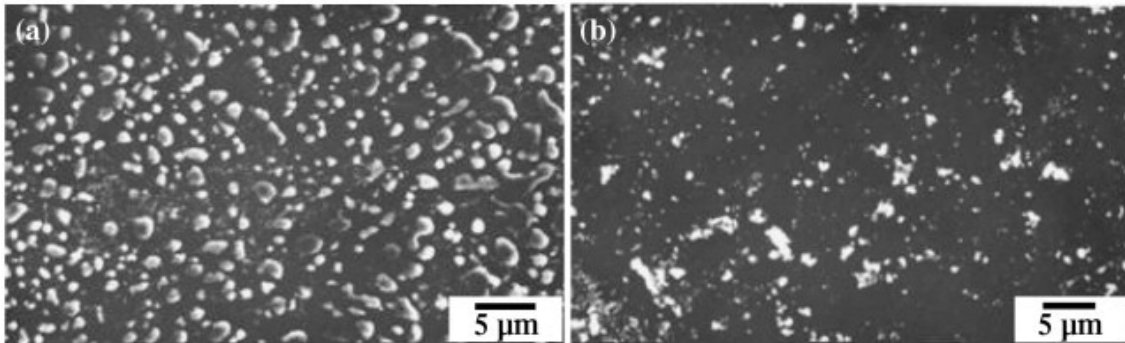


Figure 1.4: Post corrosion SEM micrograph of (a) as received steel and (b) plasma nitrided steel [13].

Fig. 1.4 displays the SEM micrographs of the as received steel and plasma nitrided steel. The micrographs show a significant reduction in corrosion on the plasma nitrided steel compared to the as received steel.

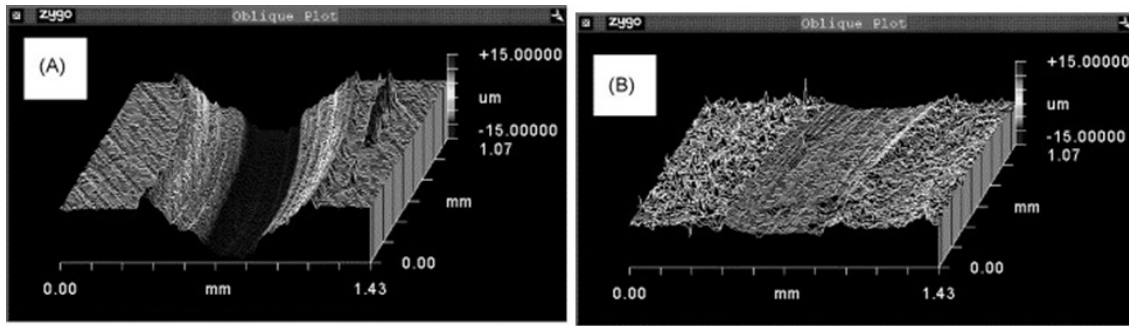


Figure 1.5: Optical profilometry of the wear tract for H13 samples at 600°C A) uncoated and B) with a gas nitrided layer [14].

Wear resistance studies using ball-on-disc tests of components treated using gas nitriding were conducted by Baracaldo on AISI H13. The optical profilometry results, displayed in Fig. 1.5, show the difference between a plain H13 surface and one that has been annealed and nitrided [14]. A clear increase in wear resistance can be seen in the gas nitrided and annealed sample.

Though many studies have been conducted on iron and steels to understand the nitride formations and effects on material properties, the knowledge basis for nitriding on zirconium and zirconium alloys is still lacking. Even on steels, it is not well known how nitride layers would stand up to reactor conditions.

2. NUCLEAR MATERIAL PROBLEMS

2.1 Fuel Cladding Materials

In a nuclear reactor, fission products produced during operation are radioactive and emit radiation that may be lethal to humans. Of the multiple barriers in place to protect the workers, the public, and the environment against the release of radioactivity from fission products, the fuel cladding is the most important. The fuel cladding safety barrier contains the majority of the radioactive fission products and a significant amount of research has gone into development of the fuel cladding [15]. Failure of the materials under accident conditions is safety concern as well as a financial concern since material problems in nuclear plants are significantly more costly than similar failures in non-nuclear plants. Therefore, the selection of materials for the fuel cladding is a crucial part of reactor design and many considerations must be taken into account.

A typical reactor fuel assembly showing how the fuel pellet and fuel rods are grouped is displayed in Fig. 2.1. A reactor may contain dozen of these fuel assemblies or bundles each of which have over 200 fuel rods. A depiction of an individual fuel rod displaying the arrangement of the pellet and cladding is shown in Fig. 2.2 [16]. Clad design considerations include working temperatures, neutron absorption cross section, thermal expansion, thermal conductivity, creep resistance and corrosion resistance under these conditions. Furthermore, the operating environment is complex and the cladding should maintain its integrity under normal and abnormal operating conditions.

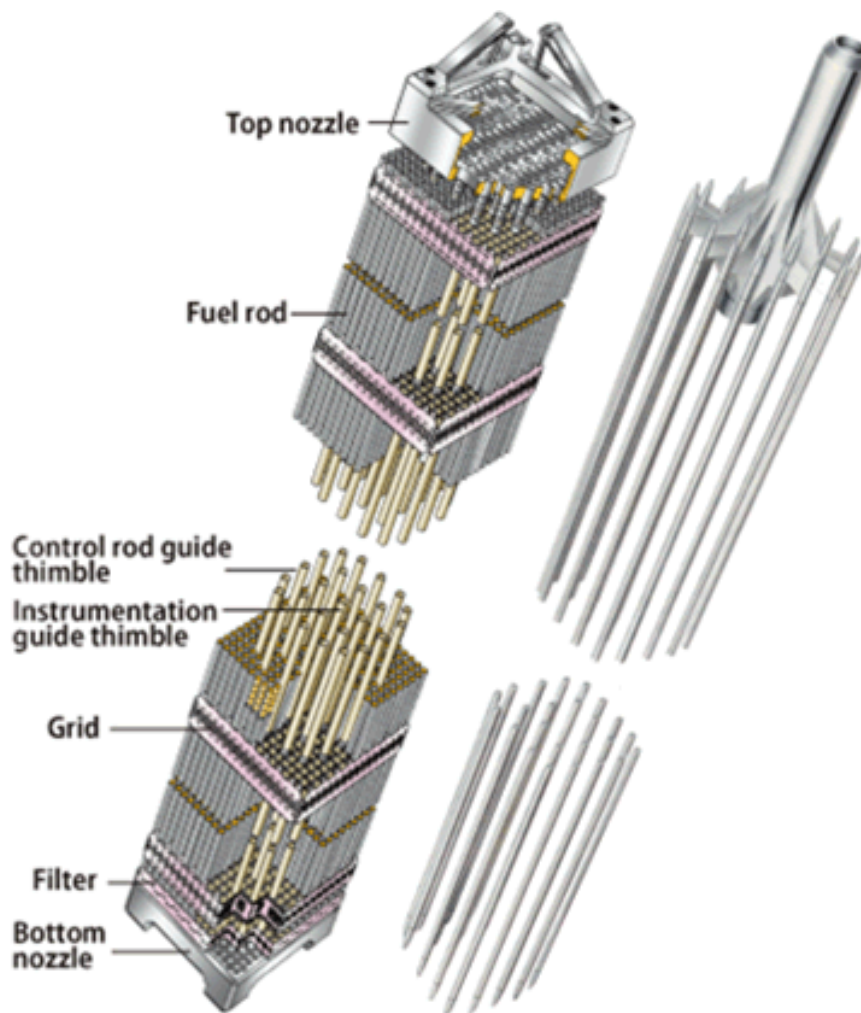


Figure 2.1: A nuclear fuel assembly with the rod cluster control assembly [16].

Zirconium alloys have been the preferred cladding material in light water reactors since the 1960s because of their low effective neutron absorption cross section, good mechanical properties, high service temperature, and corrosion and radiation resistance. Still, these alloys have limitations that must be addressed to improve reactor performance and safety. For example, at high temperatures, aqueous corrosion controls the life of PWR fuel cladding. The corrosion is normally caused by the ingress of hydrogen into the

cladding which causes degradation of the mechanical properties [15, 17]. Advancements in alloy compositions have led to only small increases in service temperatures leaving the need for further improvements.

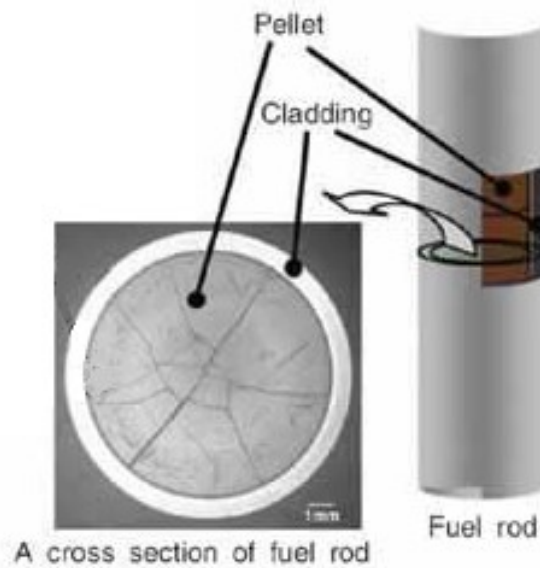


Figure 2.2: Fuel rod with depiction of pellet and cladding placement [18].

Early LWRs used stainless steels for fuel cladding, but the steel was replaced by zirconium alloys due to better neutron economy and higher melting temperatures. Austenitic stainless steels have good creep resistance at high temperatures and fair corrosion and oxidation resistance allowing them to serve as fuel cladding material for fast reactors up to 600°C. However, they are susceptible to radiation induced material problems including void swelling, He embrittlement, and irradiation creep. In relation to ferritic and martensitic steels, austenitic steels are far more prone to void swelling. Attempts have been made to increase radiation resistance through methods of trace

element doping, cold deformation, and precipitation of dispersed phases, but the challenges presented by austenitic stainless steel still remain [15].

2.2 Thermal Fatigue Cracking

There are various components of nuclear reactors that undergo thermo-mechanical loading [19]. For example, in some fast reactor designs, strong thermal fluctuations are produced by the mixing of different temperature flows of or by cyclic movement of the sodium stratification interface in pool type designs. These fluctuations can produce crack networks. PWRs may also experience thermal fatigue cracking despite the relatively small temperature fluctuations in their primary coolant loops [20].

Fatigue in metals is the result of repeated reversals of inelastic deformation. Solids must be able to be deformed by non-recoverable inelastic deformation in order to be prone to progressive failure by fatigue. If the deformation takes place in a localized spot on a microscopic scale, it will take thousands to millions of cycles to initiate cracks and crack propagation on a macroscopic scale. However, if the cyclic inelastic deformation takes place on a larger scale, only a few cycles may be required to induce failure. This is referred to as low-cycle fatigue and can also happen as the result of large strains at a constant temperature. Thermal fatigue is usually the source of deformation in low-cycle fatigue predominately because of the low frequency of thermal cycling in most engineering structures [21].

Generally in engineering systems that operate at elevated temperatures, components undergo the most severe temperature changes at the beginning and end of

operation. For example during a SCRAM, the control rods are inserted to absorb neutrons and quickly lower power levels causing a drop in temperature. Rapid changes in temperature create high thermal gradients which induce high thermal stresses and strains. The cyclic loading conditions caused by the temperature gradients are essentially deformation limited loadings. Because of this, research of thermal fatigue is generally limited to strain-controlled low-cycle fatigue tests [21].

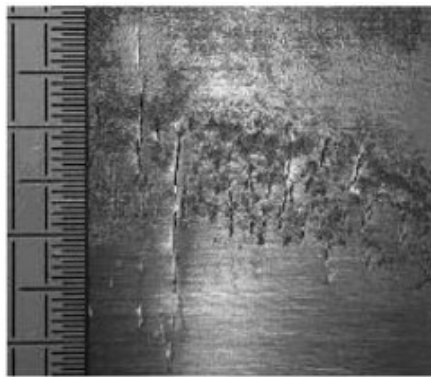


Figure 2.3: 316L steel specimen after undergoing thermal fatigue testing [21].

Thermal fatigue resistance of materials has generally been assessed by performing isothermal low-cycle fatigue tests at that estimated maximum temperature of the thermal fatigue cycle [21]. Operating for long lengths of time at a steady state elevated temperature may be simulated by holding the components at the highest expected tensile or compressive strain within the isothermal cycle. With this type of testing, long time exposure effects caused by oxidation, hot corrosion and creep could be assessed with relatively simple experiments [22]. Figure 2.3 shows a steel specimen that has experienced thermal fatigue cracking from testing.

2.3 Wear

Wear occurs as a result of the interactions between two surfaces. In wear, there is erosion and deformation of one material surface by actions of another surface such as sliding, rolling, and impact. Deformation and dimensional loss by wear is also affected by other conditions including the speed at which interactions happen and the surrounding temperature. Fretting is a particular type of wear that decreases the fatigue strength of materials under cycling stresses [23].

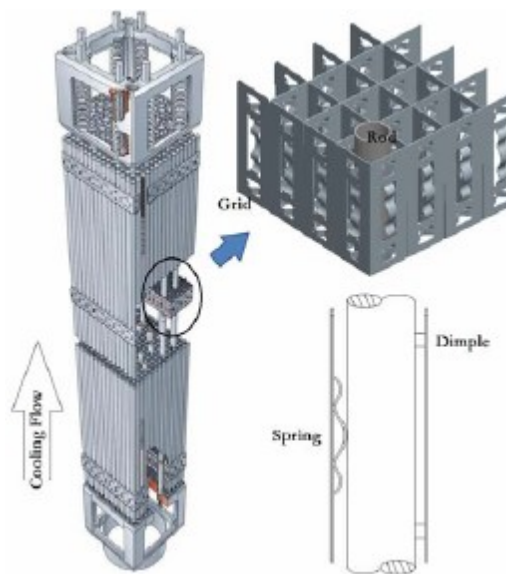


Figure 2.4 Picture of the grid-to-rod assembly [23].

In a reactor, the fuel cladding can potentially experience wear from any surface it comes into contact with including the fuel and more significantly, the grid which holds the fuel rods and debris in the coolant. The rods are supported in the grid by springs or

dimples as seen in Fig. 2.4 [23]. As the coolant in the reactor flows over the surface of the fuel rods, flow-induced vibration occurs. Fretting between the grid and rods due to vibrations is a cause of fuel cladding failure in reactors [24]. Work has been done in reactors to decrease wear by filtering debris and redesigning grid springs. Developing a more wear resistant cladding would further reduce the potential for wear failure.

2.4 Delayed Hydride Cracking

Early use of zirconium alloys found that hydrogen acted as an embrittling agent. Hydride precipitates that formed as platelets were identified as the source of the embrittlement. The embrittlement takes two forms: short term loss of toughness and a stable, time-dependent crack growth mechanism called delayed hydride cracking (DHC). In DHC, hydrides form from dissolved hydrogen in the alloy or hydrogen introduced from corrosion. The hydrides nucleate and grow slowly in high stress regions such as crack tips or notches [25]. Enough hydrides will create a brittle area leading to the formation and propagation of a crack to relieve the stress. Hydrogen then migrates through the newly formed crack to unaffected areas forming more hydrides which cause further cracking as seen in Fig. 2.5. The cycle repeats until there is an insufficient amount of metal remaining to carry the load and the cladding fails [26].

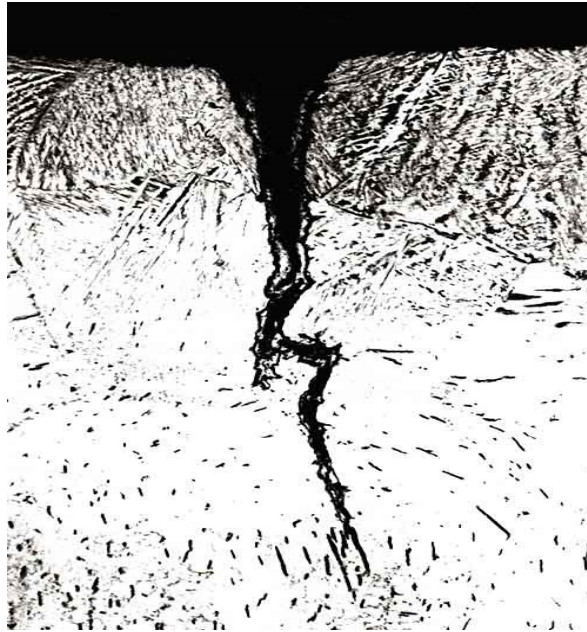


Figure 2.5 Picture of a hydride area and crack [27].

In some Boiling Water Reactors (BWRs), hydride cracking was strongly implicated in long splits in the nuclear fuel cladding that resulted in the leakage of fission products. If the cladding wall is penetrated during operation due to the aforementioned corrosion mechanisms, liquid water may enter the fuel cladding and contact the fuel surface to produce steam. Large quantities of hydrogen are then generated as the steam oxidizes the cladding. A reduction in the partial pressure of the oxygen in the steam results leaving a gas rich in hydrogen. This is sometimes referred to as oxygen starvation. The gas stream becomes almost completely hydrogen a short distance away from the defect resulting in a breakdown of the protective oxide layer on the cladding, allowing large quantities of hydrogen to be absorbed increasing embrittlement of the material [25, 26].

Because of the transient stresses associated with fuel pellet-cladding interaction during power ascension and decent, DHC in zirconium alloys has the potential to be a serious problem in the operation of nuclear plants; furthermore, DHC is a concern in the storage and disposal of high burnup fuel rods [28]. Thus, understanding DHC is critical to the safe operation of nuclear facilities and DHC prevention continues to be an important research topic.

2.5 Corrosion

When considering fuel cladding corrosion, reactions of the cladding with the nuclear fuel and its environment must be considered as well as corrosion of the outer surface which can be exposed to differing environment when in service, temporary storage, and permanent storage. Most cladding failures initiate at the inner tubing wall due to causes such as pellet cladding interactions, hydriding, and fretting. Failure on the outside of the cladding can be caused by water side corrosion and crud-induced corrosion [29].

The corrosion properties of fuel cladding materials can be adjusted by alloying. For instance, zirconium alloys have superior corrosion resistance compared to pure zirconium in high temperature water or steam. Alloying with small amount of tin, iron, chromium, and nickel improve resistance to high temperature water corrosion [29].

After the Fukushima event, which will be described in detail later, the use of stainless steels as cladding in PWRs instead of zirconium alloys has and continues to be considered. Currently, stainless steel is being considered as a replacement for zircaloy for

safety related issues related to hydrogen production and explosion potential since the stainless steel cladding has a much lower oxidation rate compared with zirconium alloys at high temperatures. Stainless steel is also more resistant to pellet cladding interactions at steady-state and under controlled transients. When compared with zirconium alloys, stainless steel is less susceptible to stress corrosion cracking from fission products in the fuel; has a lower potential for oxygen embrittlement; and, has better mechanical strength and ductility. Still, only a limited number of efforts have been made to model PWRs with stainless steel cladding [30].

2.6 Fukushima Daiichi Explosions

The 2011 explosions at the Fukushima Daiichi represent an extreme case of material problems leading to failure and the subsequent release of radioactive material. There have been a total of three severe core melt accidents in the commercial nuclear industry since the inception of nuclear power with the others being at Chernobyl, Ukraine in 1986 and at Three Mile Island, United States in 1979. These accidents, especially one so recently, show a need for improved reactor systems materials.

At Fukushima, hydrogen accumulation in the containment building may have taken place because of several reactions that followed the severe accident in the nuclear reactor. Hydrogen can build up as a result of radiolysis of water, reactions between water and boron carbide, interaction of the molten core with the concrete containment, and the oxidation of zircaloy by steam. The source able to generate significant levels of hydrogen is oxidation of the zircaloy cladding. The rate of production accelerates once cladding

temperatures exceed approximately 1200°C. Once hydrogen is released into the reactor coolant loop and associated fluid systems, it can migrate and accumulate in containment. Once a critical Hydrogen-Oxygen ratio was met, the mixture ignited leading to an ultra-high pressure shock wave resulting in severe structural damage [31].

The 2011 accident began when an earthquake measuring 9.0 on the Richter scale hit near Fukushima. Following plant safety design requirements, the reactor tripped and the power plant automatically began to initiate shutdown and core cooling processes with no apparent damage. An hour later, the plant was hit by a beyond-design-basis tsunami that disabled the emergency power supply severely impacting the emergency core cooling systems. This caused a total power black-out and destroyed the sea water pumps at the station. The lack of power meant an inability to cool the core with water. The core coolant boiled off water creating steam that raised the vessel pressure. The pressure was relieved through the Automatic Depressurization System (ADS) valves and RCIC turbine into the suppression pool. Once the RCIC turbine failed, the water level in the core began dropping to about halfway down. Simultaneously, the suppression pool became saturated and the containment pressure began rapidly increasing. Eventually, the reduced cooling from the RCIC and the subsequent uncovering of the fuel rods led to an increase in cladding temperature to approximately 1200°C. At this point, the zircaloy cladding began to rapidly oxidize in the steam environment releasing hydrogen. The temperature continued to rise and eventually the fuel and rods were completely melted [31].

Hydrogen accumulated at the roof of the reactor building which was comparably lightly plated. When the hydrogen ignited, it destroyed a large part of the roof and lateral

walls and disperse a significant amount of volatile fission products. The explosions happened first in Unit 1, then in Unit 3 and finally Unit 4. In Unit 4, which was de-fueled, the explosion is believed to have been most likely caused by back flow of hydrogen through the pipes connecting Unit 3 and 4. Less likely causes are hydrogen released from the heating and oxidation of Zircaloy in the spent fuel pool or hydrogen from the electric generator refrigeration [31].

In light of the Fukushima accident, it is important to understand the mechanisms involved with the oxidation and hydrogen accumulation that occurred from interactions with the zircaloy fuel cladding. By understanding how these mechanisms work, accident tolerant cladding can be made from treatments like nitriding to ensure the safety and reliability of reactors during severe accidents.

3. RUTHERFORD BACKSCATTERING ANALYSIS

Rutherford backscattering spectrometry (RBS) is a non-destructive ion beam technique that has variety of useful applications. The technique derives its name from Lord Ernest Rutherford whose gold foil experiment demonstrated the existence of a nucleus within an atom. Applications include composition and thickness and thin films or layers, mass and depth, element rations, crystalline quality, and lattice location of impurities in single crystals.

RBS involves bombarding a sample with an ion beam and measuring the energy and number of ions that backscatter off the near-surface region as demonstrated in Fig. 3.1 [32]. The number of backscattering events that can happen depends on the concentration of an element and the size of its nucleus. The associated probability is called its scattering cross section [33].

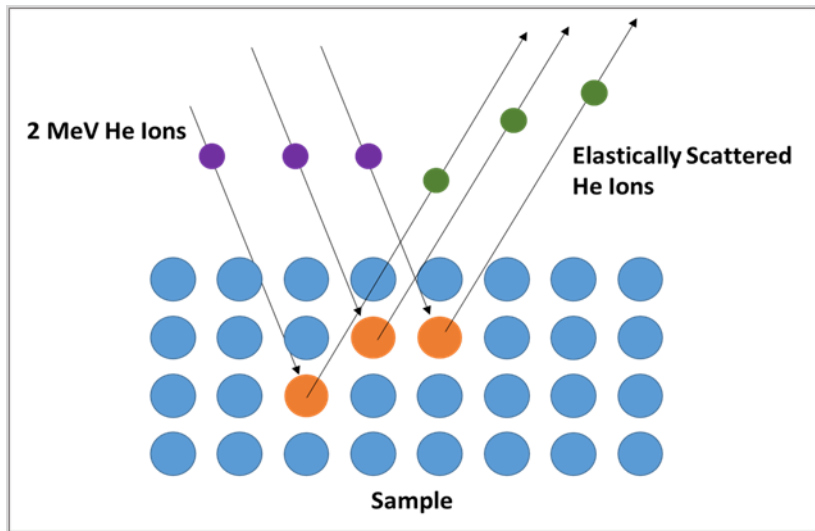


Figure 3.1 Diagram of He ion collisions in RBS.

RBS is more sensitive to concentrations of elements heavier than the main substrate element than lighter elements. The sensitivity for information about the sample deep beneath the surface is also poor. RBS is only sensitive to depth of approximately 1 or 2 μm .

Due to the small size of the nuclei compared to the empty space between nuclei in a material, the majority of incident particles do not undergo a collision in the near-surface region. The collisions that do occur can be accurately modeled as elastic collisions using Newtonian physics.

3.1 Geiger - Marsden Experiments

Rutherford started graduate work by studying the effects of x-rays on various materials. After radioactivity was discovered, he began studying the particles emitted by

uranium and uranium compounds. To study the effects of the particles on matter, Rutherford first had to find a way to count the individual particles. Eventually he found that a zinc sulfide coated screen would emit a burst of light each time it was hit by a particles. Rutherford and Hans Geiger, his assistant, could see the light by sitting in the dark until their eyes became sensitive and try to count the flashes [34].

Rutherford discovered that a thin beam of particles was broadened when it went through a thin film. Thus he had Geiger measure the angle through which the particles were scattered through a gold foil. Gold was used because its ductility allows for extremely thin foils to be made. Geiger found the scattering was about one degree as Rutherford had expected because he knew that the particles had considerable mass and moved fast. He also expected that nearly all the particles would be able to penetrate the foil with some scattering from target atom collisions [35].

Ernest Marsden, another researcher in Rutherford's lab was given the task to see if the particles could be scattered through a large angle. Marsden found that only a very small fraction of the particles were scattered through angles above 90° . To explain these results, Rutherford concluded that the positive charge and mass of an atom must be concentrated in a small fraction of the total volume. When Rutherford published the results, he proposed a model of the atom that is still used today [35].

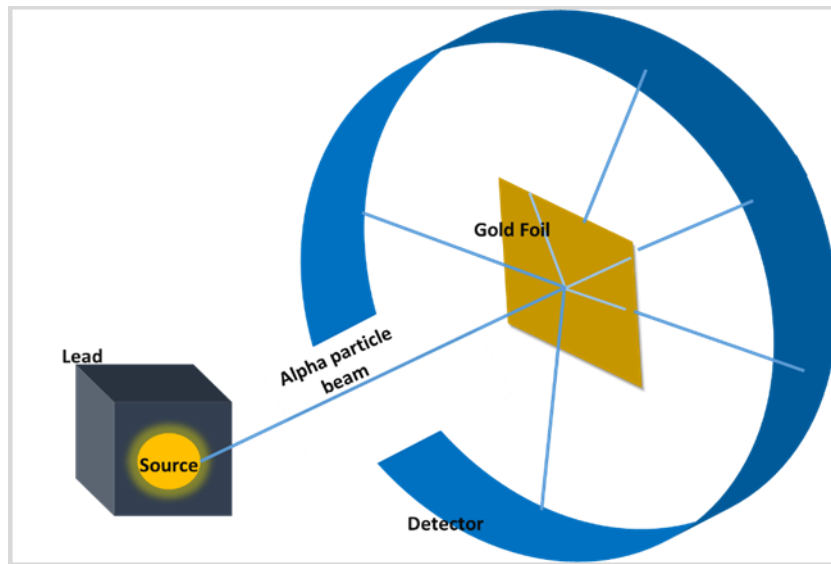


Figure 3.2: Schematic of Rutherford's gold foil experiment.

In the gold foil experiment, depicted in Fig, 3.2, most of the particles were able to go through the foil without hitting anything large enough to significantly deflect their path. A few of the particles came close to the nucleus of the gold atoms as they went through and were repulsed by the positive nucleus in a small angle. Occasionally, the particles would have a direct collision with the nucleus and be deflected through angle of 90° [35].

Through careful measurements of the fraction of the particles deflected through large angles, Rutherford was able to make an estimate about the size of the gold nucleus. By his calculations, the radius of the gold nucleus had to be at least 10,000 times smaller than the radius of the entire atom. This indicated that the overwhelming majority of an atom is empty space [34].

3.2 Theory

3.2.1 Scattering Geometry and Kinematics

The scattering geometry used for the experiments is displayed in Fig. 3.3. In this setup, the incident beam, backscatter beam, and surface normal to the sample are in the same plane. The scattering angle, θ , is defined by:

$$\theta = 180^\circ - \beta \quad (3.1)$$

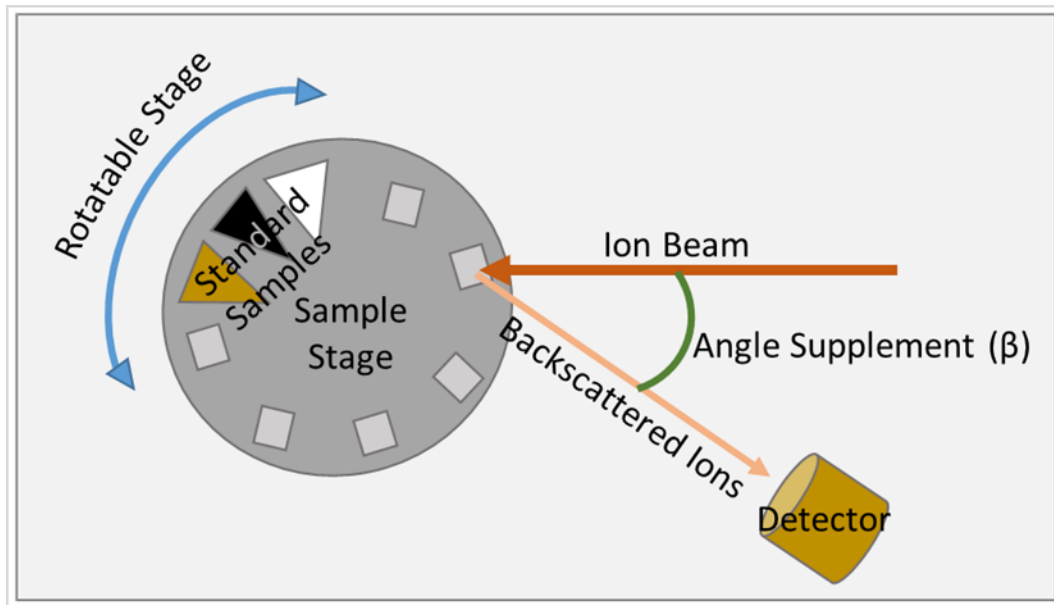


Figure 3.3: Diagram of the RBS setup used in experiments.

When a scattering event happens on the surface of the sample, the only energy lost by the incident ion is through momentum transfer to the target atom. The ratio of the ion's energy before and after the collision is defined as the kinematic factor, K , given by

$$K = \frac{M_1^2}{(M_1 + M_2)^2} \left\{ \cos\theta + \left[\left(\frac{M_2}{M_1} \right)^2 - \sin^2\theta \right]^{\frac{1}{2}} \right\}^2 \quad (3.2)$$

where M_1 is the mass of the incident ion and M_2 is the mass of the target atom. The backscatter energy, E_1 , with incident energy, E_0 , is then

$$E_1 = KE_0, \quad (3.3)$$

and the energy separation can be defined by

$$\Delta E_1 = E_0 \frac{dK}{dM_2} \Delta M_2. \quad (3.4)$$

The energy separation and mass resolution are greatest for light target elements and small for heavy elements. This can be attributed to the difference in momentum transferred during collisions. For increasingly heavy elements, less momentum is transferred to the target atom and the energy of the backscattered particle asymptotically approaches the energy of the incident particle. In terms of material analysis, this means RBS is better suited for distinguishing two light elements than two heavy elements [36, 37].

For the experiments presented in this paper, RBS was performed using a 2 MeV helium, He, beam. It is important to note that elements, in this case hydrogen, lighter than the incident beam will scatter forward, not back. Therefore, traditional RBS cannot be

used to detect these elements. Instead, techniques like hydrogen forward scattering can be used with essentially the same equipment as RBS to measure the hydrogen atoms scattered forward.

3.2.2 Scattering Cross Sections

The scattering cross section, σ_R , is related to the number of backscattered particles into a solid angle for a given number of incident ions and defined by

$$\sigma_R \left[\frac{mb}{sr} \right] = 5.1837436 \times 10^6 \left(\frac{Z_1 Z_2}{E[keV]} \right)^2 \frac{\{(M_2^2 - M_1^2 \sin^2 \theta)^{\frac{1}{2}} + M_2 \cos \theta\}^2}{M_2 \sin^4 \theta (M_2^2 - M_1^2 \sin^2 \theta)^{\frac{1}{2}}} \quad (3.5)$$

where Z_1 and M_1 are the nuclear charge and mass of the incident ion, respectively, and Z_2 and M_2 are the nuclear charge and mass of the target atom, respectively. The cross section can be approximated by proportion to the square of the atomic number of the target atom. As seen in Fig. 3.4, RBS is over 100 times more sensitive to heavy elements than light elements due to the magnitude of the corresponding cross sections [36].

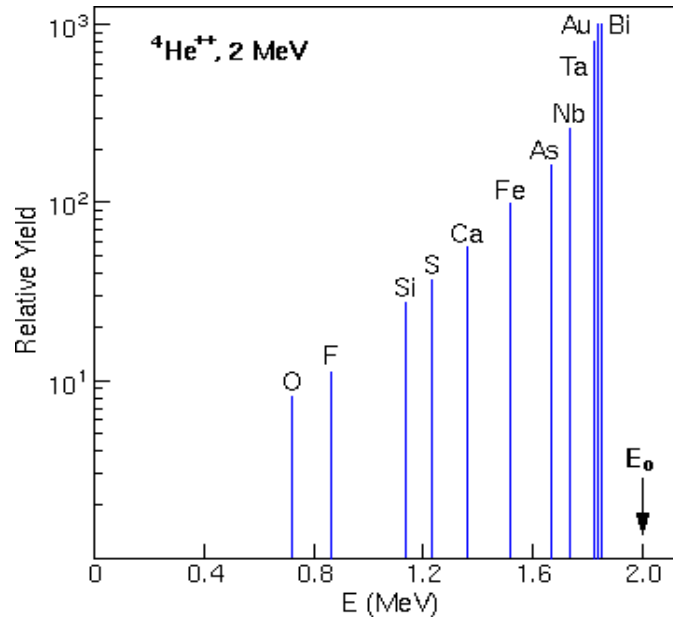


Figure 3.4: RBS sensitivity for various elements using a 2 MeV He beam [36].

3.2.3 Stopping Power

Most of the incident He ions are implanted within the sample material. Just a small percentage of the incident ions actually have a nuclear collision and backscattered. The energy of a backscattered particle depends on the energy lost by interactions with electrons (electronic stopping power) and interactions with nuclei (nuclear stopping power). The further an ion travels into the sample before being backscattered, the less energy the backscattered ion will have. The amount of energy that is lost depends on factors including the ion's initial velocity, the elements in the sample material, and the density of the sample material. For a 2 MeV He beam, the energy loss is typically between 100 and 800 eV/nm. This energy loss can be used to accomplish depth profiling or measuring layer thicknesses [37].

Electrons slow down the He ions by inelastic collisions in a process that behaves similarly to frictional stopping. The energy loss by incident ions is predominately from electronic stopping. Thus, the electronic structure of the target material has a high impact on the overall stopping power. Nuclear stopping which is the result of glancing collisions along the path of the incident ion are only significant at very low incident energies [36, 37].

The physics behind energy loss phenomena are complex. Thus, theoretical predictions are also complex and inaccurate. Stopping powers used in RBS are therefore usually taken from empirically data. A polynomial equation and table of coefficients provide a way to calculate stopping powers over a wide range of energies and elements. Energy loss per unit of depth can be calculated by multiplying the stopping cross section by the density of the sample material. The densities of various materials vary widely, so sample density must be known to calculate the depth of a feature or layer thickness [37].

3.2.4 Calibration and Layer Thickness

Before data acquisition can begin when performing RBS, a calibration of the detector must be done. To do this at least two samples of known mass and composition must be used. For the experiments in this work, gold and silicon were used. By utilizing Eq. 3.2, the K-factors of these standards can be calculated. Then a spectrum of the two standards can be acquired, and the channels of the silicon and gold, Ch_{Si} and Ch_{Au} respectively, at the leading edges located [36, 37].

$$E_0 K^{Si} = k SCh_{Si} + Z_0 \quad (3.6)$$

$$E_0 K^{Au} = k SCh_{Au} + Z_0 \quad (3.7)$$

$$k = E_0 (K^{Si} + K^{Au}) / (SCh_{Si} - SCh_{Au}) \quad (3.8)$$

$$Z_0 = E_0 (K^{Si} SCh_{Au} - K^{Au} SCh_{Si}) / (SCh_{Au} - SCh_{Si}) \quad (3.9)$$

Once the channels of the two standards are identified, it is possible to use a linear relationship to determine what masses correspond to each channel. By using Equations 3.6 and 3.7, k and Z_0 can be solved for and plugged into Eq. 3.10 to find the relationship between channels and energy.

$$E = k(Ch) + Z_0 \quad (3.10)$$

Finding the thickness of a layer, like the tungsten/silicon in Fig. 3.5, can simply be done by measuring the energy width, or channel width and converting to energy, of the W peak or Si step and dividing it by the energy loss of He per unit depth in WSi.

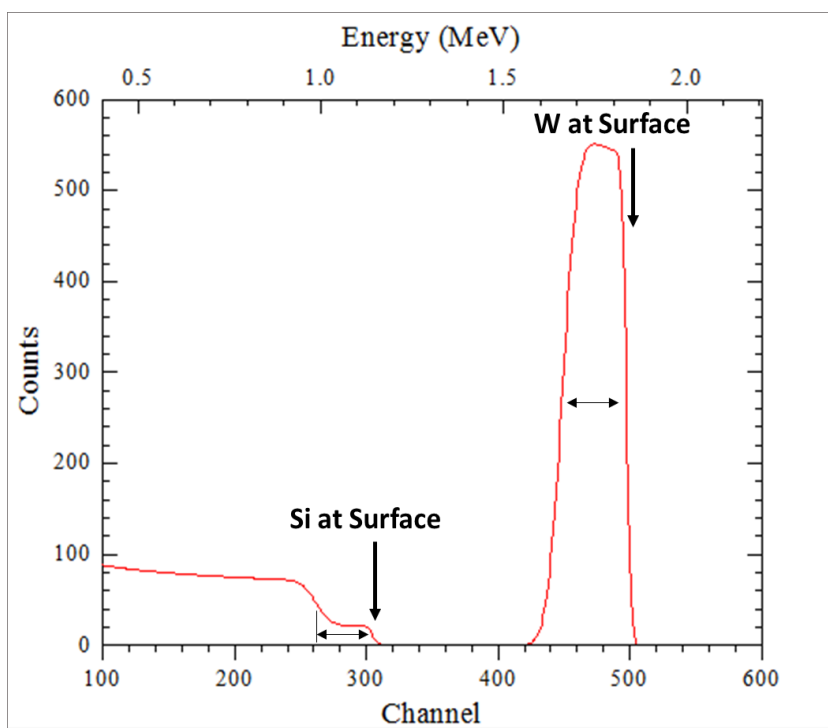


Figure 3.5: Simulated RBS spectrum of a WSi layer on a Si substrate [38].

The elemental ratios of the layer can also be determined by measuring the heights of the element peaks and normalizing to the scattering cross section of each element [36].

3.2.5 Straggling

Once the He ions pass through a target medium, they will interact and lose energy differently depending on the interactions with the target atoms. For instance, one ion might directly collide with a target nucleus and be backscattered while another ion may have several glancing collisions before being backscattered. This process is commonly referred to as energy straggling. The resulting fluctuations in the energy loss process resulting from the various trajectories of each ion, along with inherent limits of energy resolution in RBS

detection, limit the energy resolution that can be achieved for atoms that backscatter deep within the sample. This limits the depth and mass resolution for those atoms [36, 37].

As previously stated, most of the energy loss for the He ion occurs from electron interactions. Because of this, energy straggling will increase with atomic number (or number of electrons). Energy straggling results in sloping of the low energy peak edges. Straggling should be considered when evaluating a spectrum so as not to confuse the sloping from straggling with diffusion between layers (which can also produce a slope in the spectrum). The accuracy of the calculated straggling largely affects the accuracy of the depth resolution [37].

3.2.6 Density Effects

Incident He atoms lose finite amounts of energy with each encounter in the sample medium. Thus, the spacing or density of atoms will directly affect the amount of energy lost by a He atom versus the depth it travels. This density effect becomes an important factor when considering samples where the density of the deposited layer can be significantly different than the bulk material. In cases such as these, one must consider the deposited layer density to evaluate the RBS results. A convenient way of presenting RBS results is in the form of concentration of an element in the sample versus depth. Density assumptions are often made in order to present the spectrum in this way since the density of the compound layer is often unknown. However, these assumptions can cause inaccuracies in an analysis and so must always be stated and taken into account for the overall error [36].

3.2.7 Channeling

In addition to determining element compositions, RBS can also be used to study the structure of crystalline materials. In an RBS spectra, the signal peak of an impurity in the bulk material lattice is separated by scattering kinematics. The bombarding He ions will backscatter from the first few monolayers of the material at the same rate for aligned and non-aligned samples; however, the backscattering from atoms buried in the lattice will be significantly lower for the aligned sample since the atoms several layers below the surface are essentially blocked. As an example, the backscattering signal amplitude from a single crystal silicon sample that is channeled along the $\langle 1-0-0 \rangle$ axis will be about 3% of the backscattered signal amplitude from a non-aligned sample. By measuring the difference in backscattering it is possible to quantitatively measure and profile crystal structure and orientation. [36].

3.3 RUMP

Data analysis for RBS is relatively straightforward and only requires the data spectrum and simulation software like RUMP (the acronym has no specific meaning). RUMP is an ANSI C based program specifically designed for analysis and simulation of RBS data. The original FORTRAN code for RUMP was developed at Cornell and has since been contributed to by other researchers at Cornell as well as other sites. Figure 3.6 below shows RUMP user interface with a sample spectrum [38].

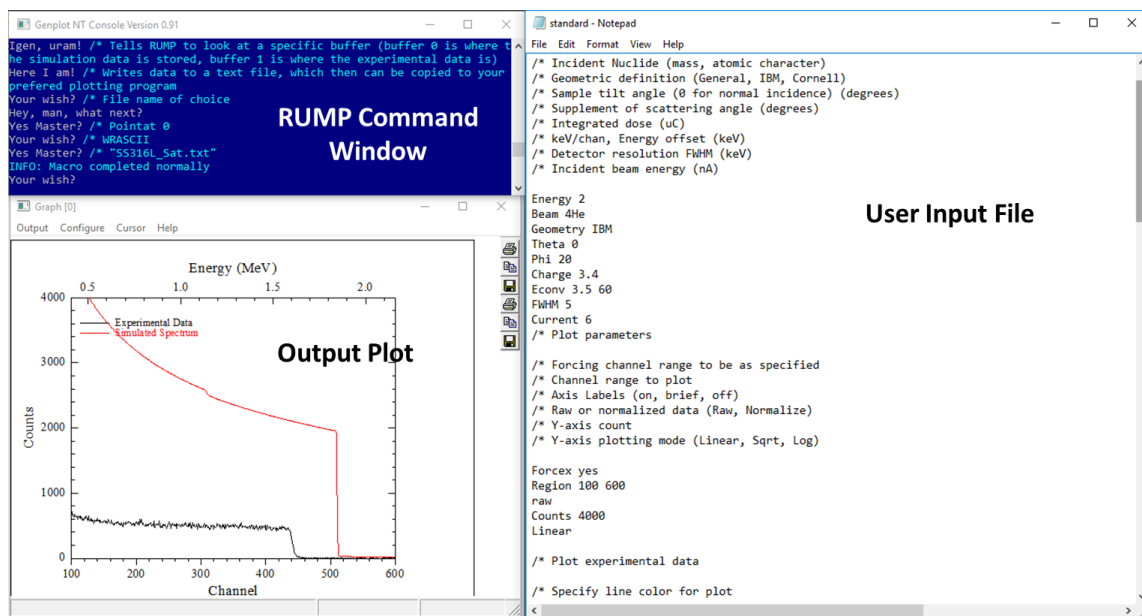


Figure 3.6: Picture of typical user interface with RUMP software [38].

To use RUMP, data files from the RBS acquisition must be imported into and saved as RUMP compatible files. Then a simulation file can be created specifying the experiment parameters including beam energy, species, sample holder tilt, detector angle, energy calibration, and energy resolution. The imported experimental data is then entered along with the nominal layer conditions. A plot of the experimental data and the simulation can be viewed using the software. The number of layers along with the composition, thickness and diffusion of each layer can be successively modified until the simulation fits the experimental. The detailed process for this is shown in the Appendix A. [38].

3.4 Equipment

For work described herein, RBS was carried out using a 1.7 MV tandem accelerator. A simplified schematic of the accelerator is displayed in Fig. 3.7. The accelerator has two different source heads, one for solid sputtering and one for gases. For solid sputtering, a solid cathode of the desired material is inserted into the Source of Negative Ions by Cesium Sputtering (SNICS) source. Cesium is used to sputter the cathode, the sputtered material is ionized and accelerated to the low energy magnet. For gases, a chosen gas is fed into the Duoplasmatron source where the gas is ionized by a filament. The ionized gas is then sent through a sodium charge exchange canal and accelerated to the low energy magnet. After the low energy magnet, the beam process is the same. The low energy magnet bends the ion beam and filters out unwanted particles. The filtered, now negative, ion beam is then accelerated in the first part of the tandem acceleration. Ions are then sent through a charge exchange canal, where the ion is stripped of electrons and becomes positive and is accelerated again. At the high energy magnet, the beam is bent to the desired chamber and further filtered.

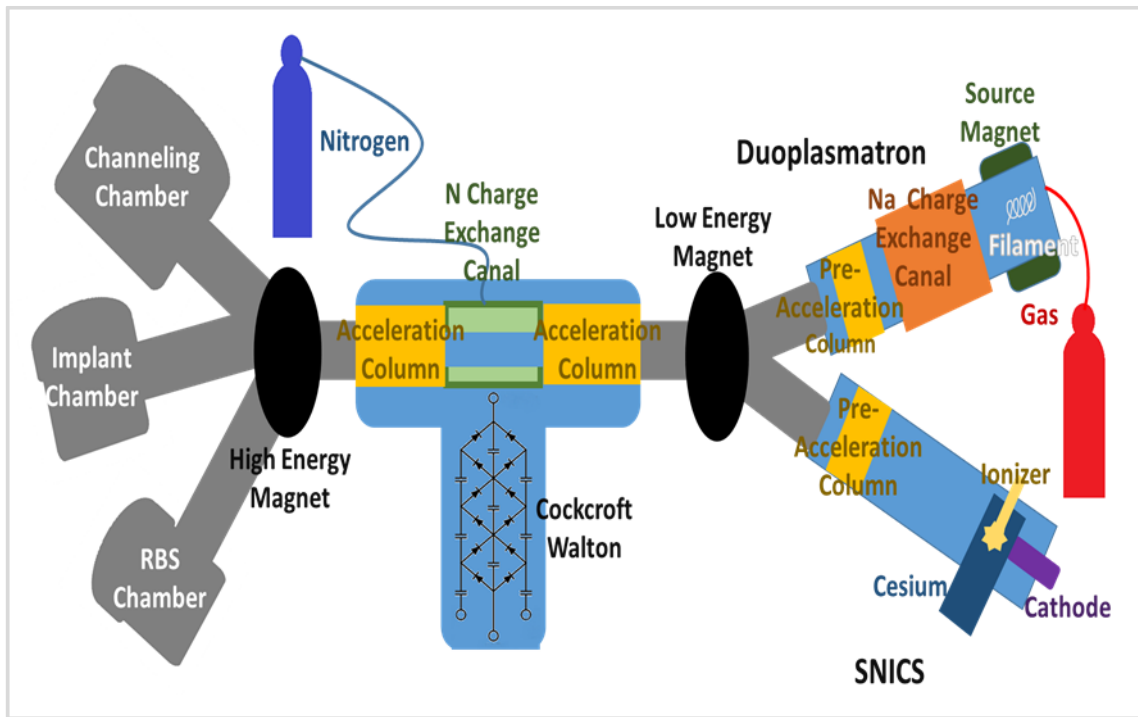


Figure 3.7: Simplified diagram of 1.7 MV tandem accelerator used for RBS.

For the RBS performed in the experiments presented here, helium gas was used with the Duoplasmatron source. Most of the RBS was performed using the RBS chamber, but some analysis was done with the channelling chamber.

4. EXPERIMENT DESIGN

Experiments were performed to understand how the nitride layers evolve within each material with increasing nitrogen dose and at what dose the samples become saturated with nitrogen. This was done by irradiating samples of each material to different doses. Further experiments were done to see how temperature affects the nitride layer. Temperature studies were completed by irradiating samples of each material to saturation and post annealing at increasing temperatures. To analyze the samples, RBS analysis was employed along with microhardness testing. Hardness testing also allows for a general idea of the wear resistance since the two properties are usually related.

4.1 Materials

Zircaloy-4 and SS316L were chosen because of their use as nuclear fuel cladding materials. As previously mentioned, zircaloy-4 is common as cladding in LWRs and SS316L is common in fast reactors as well as various LWR reactor vessel internal components. Iron and zirconium were chosen as they are the base materials for zircaloy and stainless steel. The composition of zircaloy-4 and SS316L by elements are Zr, Sn 1.2-1.7%, Fe and Cr 0.36 – 0.61% and Fe, <0.03% C, 16-18.5% Cr, 10-14% Ni, 2-3% Mo, <2% Mn, <1% Si, <0.045% P, and <0.03% S respectively.

4.2 Sample Preparation

The sample preparation was carried out in batches. It is important to note that all the samples for each material were cut and polished in the same batch with similar conditions in order to ensure as close to as identical surfaces as possible.

The pure iron samples were cut from iron bar stock using an abrasive cutting wheel. The iron was then mechanically polished with silicon carbide grit paper and DI water from 600 to 4000 grit. The final polish was done using a 0.05 μm alumina slurry and polishing pad. After polishing, the samples were cleaned in an ultrasonic bath of acetone and rinsed with DI water and methanol to remove any remaining residues.

For the SS316L samples, the same method was employed for cutting and polishing. In order to further improve the quality of the surface for transmission electron microscopy (TEM) studies, the samples were also electrochemically polished in a mixture of perchloric and acetic acid.

Samples for the zirconium and zircaloy-4 were cut in the same method as the iron and steel. They were then mechanically polished with silicon carbide paper and ethanol (water would cause surface oxidation) from 600 to 4000 grit. Due to the samples' susceptibility to retaining alumina particles in the surface, the samples could not be finely mechanically polished. To compensate for the rougher mechanical polish, the electrochemical polish was done in a stronger solution for a longer period of time.

4.3 Irradiation and Annealing

After preparing the samples, nitrogen was implanted using a 140 KV particle accelerator. A simple schematic of the 140 KV accelerator is displayed in Fig. 4.1. The samples were kept at a high vacuum, $< 1\text{E-}6$ torr, to prevent contamination during irradiation and during annealing. The 140 KV was chosen because of its ability to create relatively low energy beams which would deposit ions in the near surface region of the material.

The beam parameters used for all the samples was 80 KeV with N_2^+ ion clusters. The beam was rastered to ensure uniform irradiation of the samples. Diatomic nitrogen was chosen to further lower the energy of the ion beam (80 KeV N_2^+ corresponds with the energy of 40 KeV N^+) while remaining at a high enough energy that reasonable fluences could be obtained with this accelerator. This energy is similar to the energies used in previous research to allow for data comparison.

For the dose dependence tests, four samples were placed on the irradiation stage at the same time. Once a dose of $1\text{E}17$ N/cm^2 had been reached, the chamber was vented with nitrogen and one sample was removed. Then the chamber was put back under vacuum and the remaining samples were irradiated to $5\text{E}17$ N/cm^2 and the venting process was repeated with another sample removed. This continued for $1\text{E}18$ N/cm^2 and finally $2\text{E}18$ N/cm^2 . This method was used for all four materials.

For the temperature stability tests, four of the samples of the same material were placed on the irradiation stage and irradiated to the saturation limit. This was done for

each of the four materials. The samples were then annealed at various temperatures. The samples were annealed in the same vacuum chamber used for the irradiations.

4.4 Equipment

The 140 KV particle accelerator used for irradiation was assembled from various accelerator parts. As seen in Fig. 4.1, the system consists of a source head, acceleration column, magnet, rastering magnet, and chamber. Gas is fed into the chamber where it is ionized by a heated tungsten filament. The ionized particles are confined and shaped by the source magnet and anode to form a plasma. The beam is then sent down the acceleration column and to the magnet. At the magnet, the beam is filtered for the desired ion beam and directed down the beamline. After the magnet are rastering magnets which can be controlled by a wave generator to perform uniform scans across samples surfaces. The beam then reaches the chamber where it irradiates the given sample.

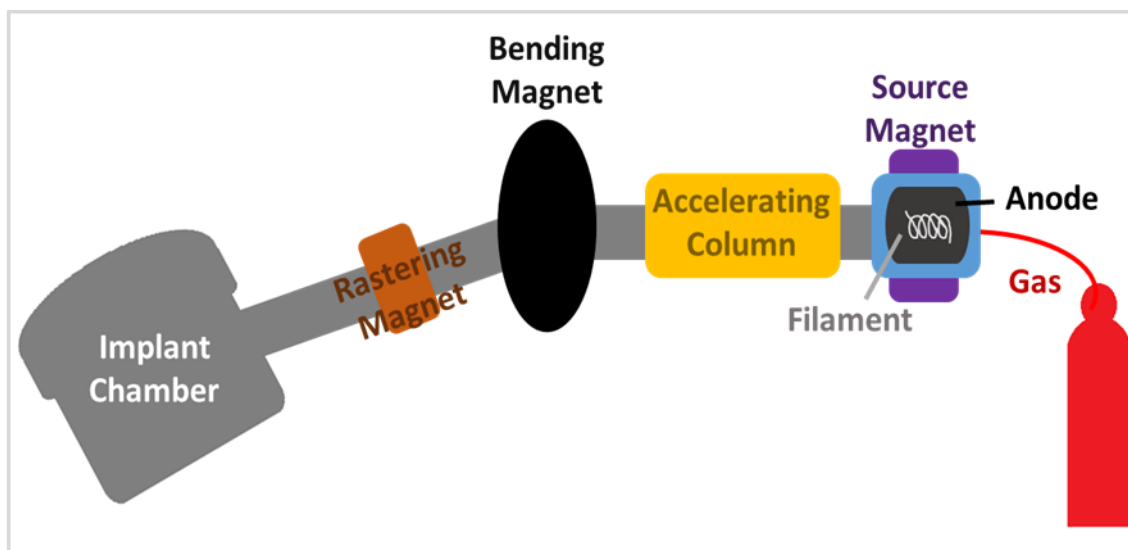


Figure 4.1: Simplified diagram of the 140 KV particle accelerator.

At the chamber, a removable metal stage is suspended in the center. Samples are attached to the surface by adhesion using silver paste, for heated irradiations, or copper tape, for room temperature irradiations. Inside the stage is a light bulb which can be attached to a variable transformer to heat the stage. The stage can reach temperatures up to 800°C.

Not depicted in the diagram of the accelerator is the vacuum system. This system is crucial to the operation of the accelerator since a beam can only be formed and used at low vacuum and to prevent contamination during irradiations. Located between the acceleration column and magnet is a diffusion pump. This pump vacuums down the source and beam line and is backed by a mechanical oil pump.

A turbopump is attached to the beamline and can be used to improve vacuum on the beamline for better beam transmission and less beam neutralizing. This turbo is backed

by a scroll pump. Attached to the bottom of the target chamber is a cryopump. This pump does not need to be backed by a roughing pump since it absorbs particles. However, it does become full after several uses and must be allowed to heat up and evaporate off particles.

4.5 Data Acquisition

Data on the samples was acquired using RBS and a nanoindenter. The RBS, which is explained in detail in section 3, was performed using the 1.7 MV tandem accelerator. An incident He beam at an energy of 2 MeV was used. The samples were placed on a stage with a goniometer to rotate between each acquired spectrum. A silicon surface barrier detector was used at an angle of 160° . The data acquired by RBS was analyzed using the RUMP software.

The hardness of the materials was acquired using a Hysitron TI 950 Triboindenter. For all samples, the nanoindenter used a force of 1mN which is at a depth of approximately 100 nm for iron. Hardness testing was performed on samples of each material that were irradiated to different doses and annealed at different temperatures.

5. IRON AND SS316L

In this section the study of the dose dependence and temperature effects on iron and SS316L are reviewed. The experiment parameters and setup are discussed in detail in the previous section.

5.1 Dose Dependence Results

The RBS spectra taken of the iron samples bombarded with Nitrogen, shown in Fig. 5.1, indicate that nitrogen initially collects closer to the surface of the sample and then diffuses back until it reaches its saturation profile. The saturation limit for iron is reached by $5E17$ N/cm².

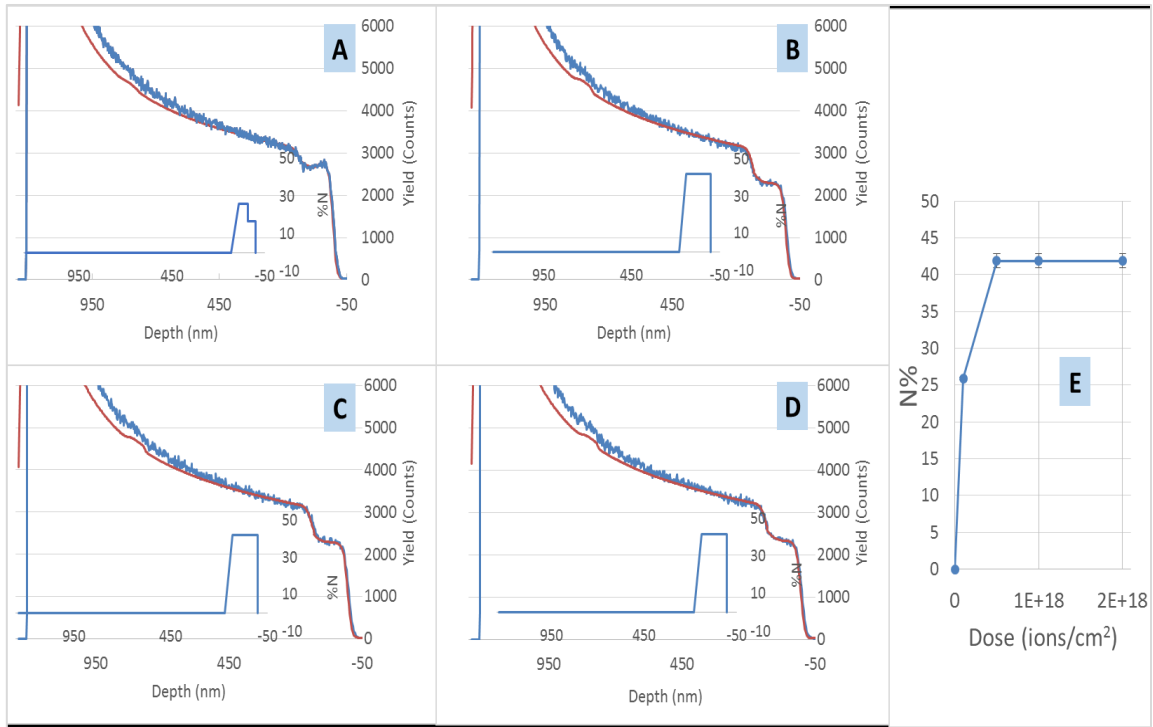


Figure 5.1: RBS spectra and associated nitrogen profiles of pure iron irradiated to A) 1E17 N/cm², B) 5E17 N/cm², C) 1E18 N/cm², D) 2E18 N/cm² and E) the concentrations plotted for each dose.

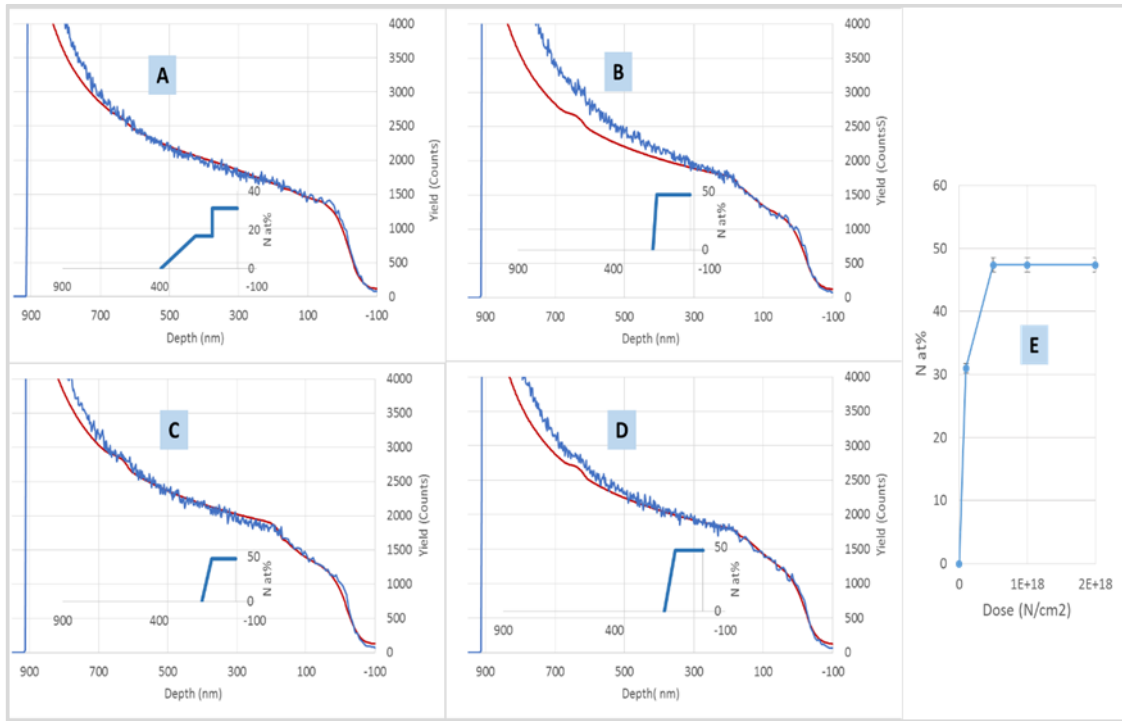


Figure 5.2: RBS spectra and associated nitrogen profiles SS316L irradiated to A) $1\text{E}17$ N/cm^2 , B) $5\text{E}17$ N/cm^2 , C) $1\text{E}18$ N/cm^2 , D) $2\text{E}18$ N/cm^2 and E) the concentrations plotted for each dose.

For SS316L the results, displayed in Fig. 5.2, are similar to iron in that the nitrogen initially collects near the surface and then begins to diffuse further into the sample. Differences between SS316L and iron appear at $1\text{E}17$ N/cm^2 as the nitrogen has diffused further back in SS316L. By $5\text{E}17$ N/cm^2 the SS316L has also reached its saturation limit.

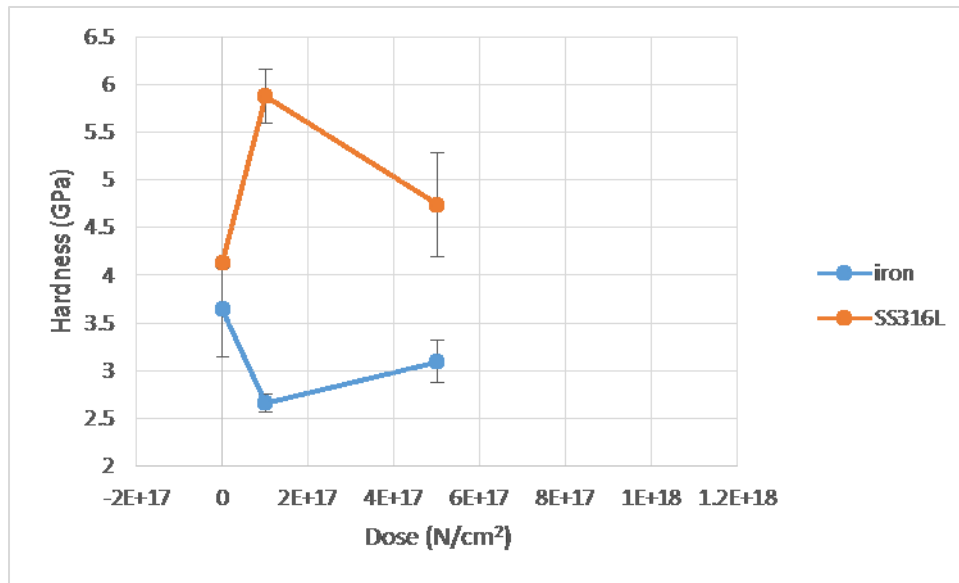


Figure 5.3: Hardness of iron and SS316L at increasing doses.

Figure 5.3 shows the progression of hardness with increasing dose. For SS316L, increasing the dose increases the hardness to a point. Past that maximum, further nitrogen implantation decreases the hardness. Increasing the amount of nitrogen in iron at room temperature does not appear to increase the hardness. Testing by Fujihana however shows a similar trend to that of the SS316L where the hardness has increased by $1E17 \text{ N/cm}^2$, but begins to decrease the hardness afterward [39].

5.2 Temperature Stability Results

Pure iron samples were irradiated at beam conditions previously stated until saturated. They were then annealed at various temperatures to see the temperature stability. The results shown in Fig 5.4 show that up to 100°C , no nitrogen is lost from annealing. As the iron is heated from 100°C to 300°C most of the nitrogen diffuses out.

Further heating to 500°C results in further loss of nitrogen. However, at 500°C there is still trace amounts of nitrogen left.

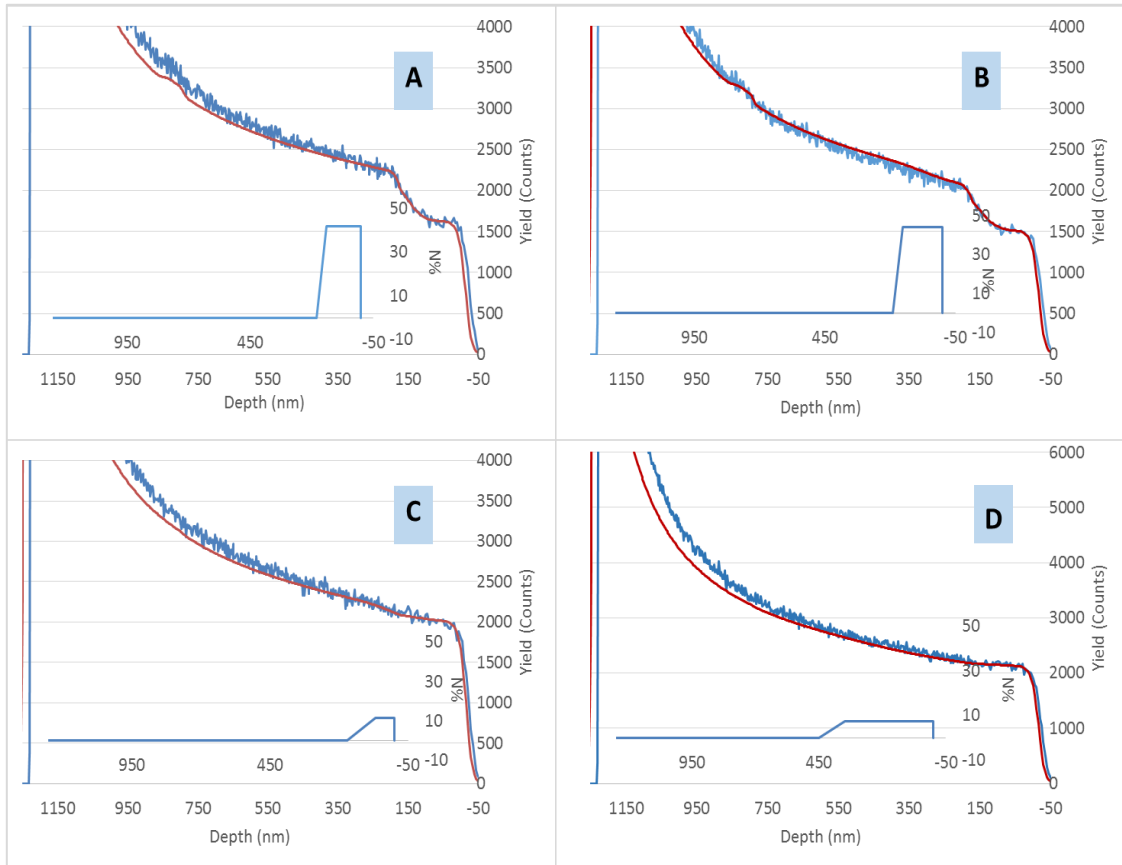


Figure 5.4: RBS spectrum of saturated iron post annealed at A) room temperature, B) 100°C, C) 300°C, and D) 500°C.

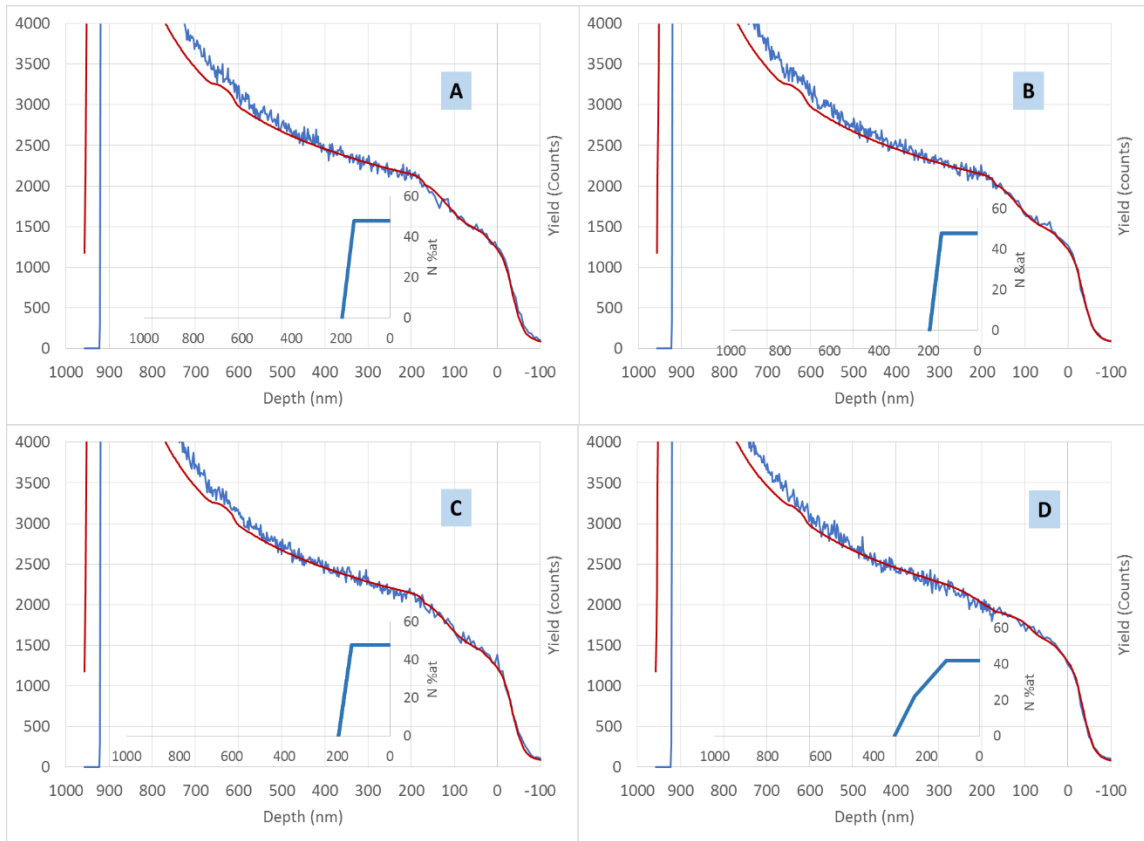


Figure 5.5: RBS spectrum of saturated SS316L post annealed at A) room temperature, B) 100°C, C) 150°C, and D) 300°C.

The RBS spectrum of annealed SS316L in Fig 5.5 shows that no nitrogen is lost indicating that all formed nitrides are stable to 150°C. By 300°C, the nitrogen content has significantly decreased indicating that some of the nitrides formed are unstable above 150°C. However, SS316L retains much more nitrogen at 300°C suggesting its nitrides are more stable at higher temperatures than iron.

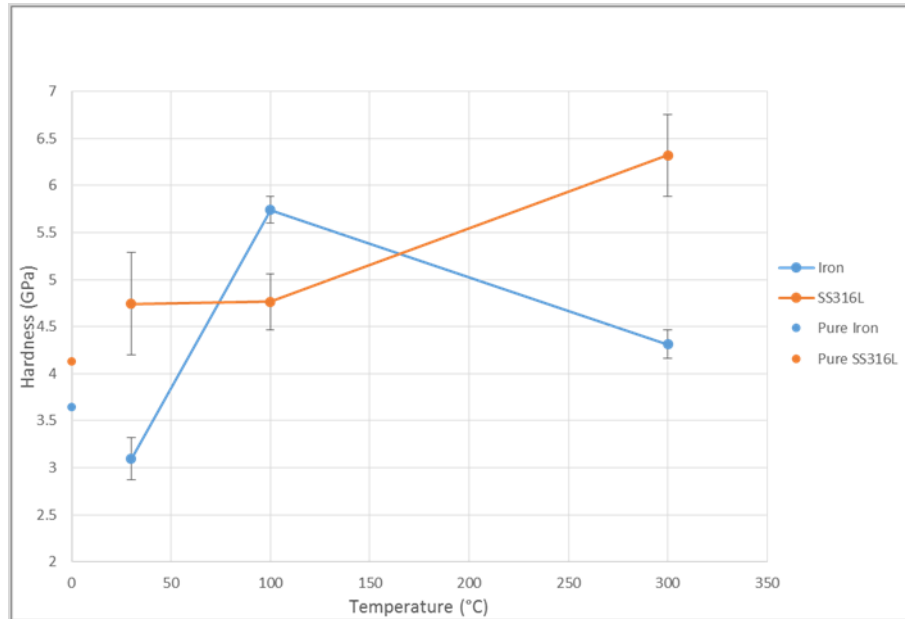


Figure 5.6: Hardness of iron and SS316L at increasing temperatures.

The hardness results in Fig. 5.6 indicate that by annealing iron at low temperatures, the hardness can be significantly increased. Annealing at higher temperatures such as 300°C where there are still nitrides present will still give an increase in hardness compared to pure iron. However, this hardness value is lower than what can be achieved at a lower annealing temperature. This phenomena is likely due to the fact that more nitrogen is retained at lower temperatures.

For steel, annealing at 100°C does not have an effect on the hardness compared to room temperature; however, at 300°C, there is a sharp increase in hardness. Unlike iron, the SS316L retains most of the nitrogen at 300°C which follows the observations stated above.

5.3 Characterization of Nitrides in Saturated Iron

To characterize the types of nitrides formed in the nitride layer of pure iron TEM was used. The sample used for this study was the $5E17 \text{ N/cm}^2$ pure iron sample irradiated at room temperature. The sample preparation done by polishing and irradiation is explained in section 4. In order to be viewed under TEM, the sample must be electron transparent. Therefore further preparation had to be done to cut out a small, thin sample from the bulk sample. This was accomplished with a focused ion beam (FIB).

The FIB system combines a scanning electron microscope (SEM), goniometer, sample manipulator, platinum deposition system, and gallium beam. The SEM is used to view the samples and the cutting and thinning process. The process for preparing a TEM sample involves first finding a clean, flat spot on the bulk sample. Then a layer of platinum is deposited on the area to protect the sample from the gallium beam. Trenches are cut on either side of the platinum using the gallium beam. The sample is slightly thinned and cut on the bottom until nearly separated from the bulk. A probe is attached to the sample through platinum deposition. The gallium beam finishes the cut separating the sample from the bulk. The probe moves the sample to a copper grid. The platinum is used to attach the sample to the grid. The gallium beam then cuts the probe from the sample. The energy of the gallium beam is lowered and final thinning is done. The sample is ready to be used in TEM [40].

TEM uses an electron beam to resolve nano-scale features in a sample. This is accomplished by focusing an electron beam and directing it through the sample. As the electrons pass through the sample, they are perturbed by the structure within the sample.

The beam is expanded onto a detector array which records an image of the perturbed beam. By utilizing this process, TEM can produce micrographs of crystal grains, dislocations loops, voids, and other microstructure features [40]. High-resolution transmission electron microscopy (HRTEM) is an imaging mode of TEM that allows direct imaging of the atomic structure of the sample.

Fig. 5.7a shows a cross sectional view of pure iron implanted to 5×10^{17} N/cm² at room temperature. Area 1 marks the area in the sample implanted with nitrogen while area 2 refers to the unirradiated iron bulk. The diffraction pattern collected from area 2 and along the [111] axis of the matrix can be seen in Fig. 5.7b. The diffraction pattern confirms the Body-Centered Cubic (BCC) structure of bulk iron. Fig. 5.7c is a HRTEM micrograph from the same region and Fig. 5.7d is the corresponding fast-Fourier (FFT) pattern which is indexed to be in agreement with BCC iron. Fig. 5.7e is a high resolution TEM micrograph from area 1 at a [331] zone axis. The micrograph shows nano-precipitates embedded in the BCC iron matrix. Fig. 5.7f is the inverse FFT pattern which suggest coherency of crystal alignments between the nano-precipitates and iron matrix. Fig 5.7g. is the corresponding FFT pattern which indicates the presence of Fe₃N precipitates.

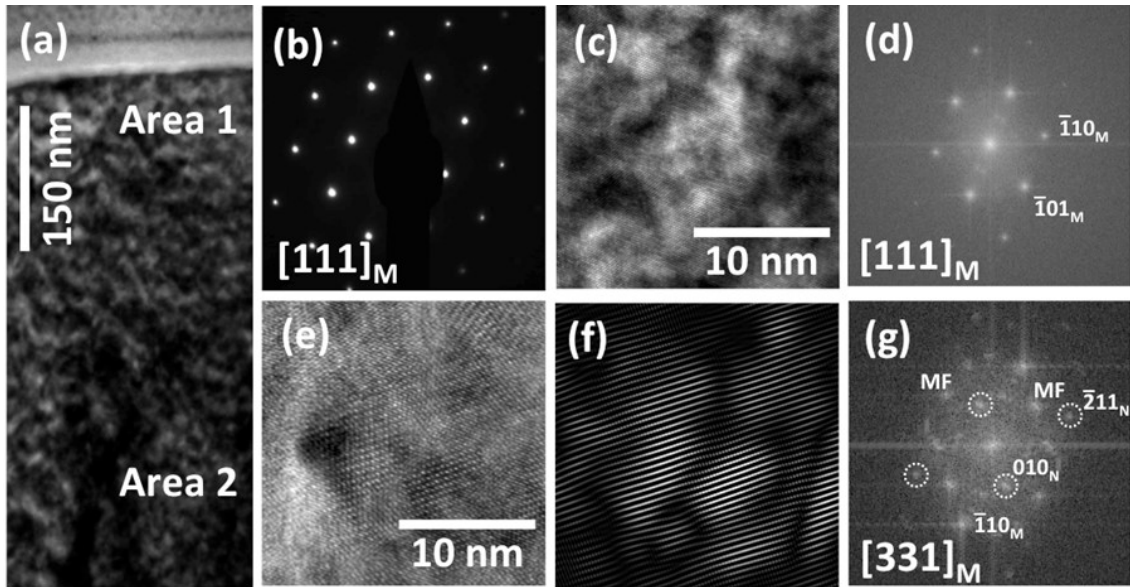


Figure 5.7: TEM micrographs of (a) a cross sectional view of 5×10^{17} N-implanted Fe at room temperature with “Area 1” referring to N implanted region and “Area 2” referring to un-implanted region, (b) the diffraction pattern of area 2, (c) a HRTEM obtained from area 2 at the $[111]$ matrix zone axis, (d) the FFT pattern of (c), (e) a HRTEM obtained from area 1 at the $[331]$ matrix zone axis, (f) the inverted FFT pattern of (e), and (g) the indexed FFT pattern of (e) with the circles referring to the diffraction spots used to construct (e).

Another nitride phase was found in addition to Fe_3N . The HRTEM micrographs of the other phase agrees with the theoretically predicted FeN_2 crystal structure. The evidence of this crystal structure in the nitrided iron is shown in Fig. 5.8. Fig. 5.8a is a HRTEM micrograph obtained at the $[111]$ matrix zone from area 1, Fig. 5.8b is the corresponding inverse FFT, and Fig. 5.8c is the corresponding FFT diagram. The circled diffractions spot in Fig. 5.8c were used to construct the Fig. 5.8b. Fig. 5.8d shows a schematic of the theoretical FeN_2 crystal structure. Fig. 5.8e compares the inverse FFT micrograph with the corresponding projected view of FeN_2 atom positions. Fig. 5.8f is a simulated diffraction pattern of BCC iron at the $[111]$ and FeN_2 at the $[1\bar{1}\bar{2}]$ zone axis. The agreement

between Fig. 5.8f and Fig. 5.8c indicate the formation of the FeN₂ phase. The measured lattice parameter of FeN₂ is 8% larger than the 2.0075 nm predicted by calculations.

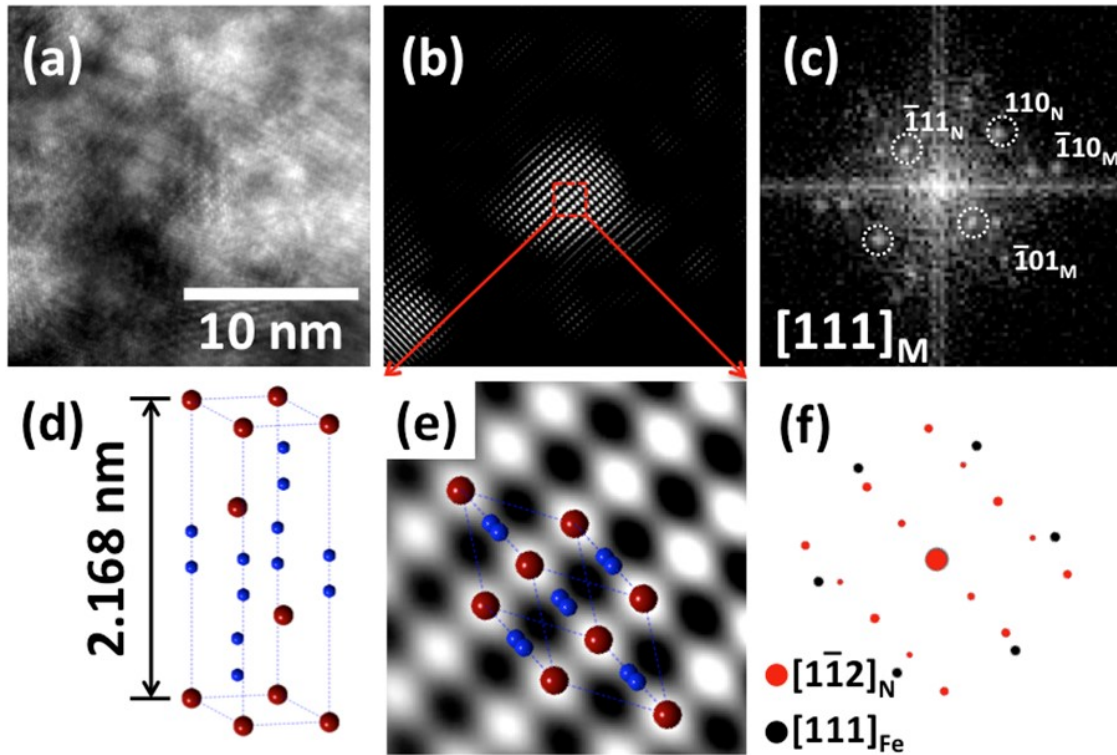


Figure 5.8: TEM micrographs of (a) a high resolution cross sectional view of 5×10^{17} N-implanted Fe at room temperature, obtained from N-implanted region, (b) the corresponding inversed FFT pattern, (c) the corresponding indexed FFT pattern with the circled spots used to construct (b), (d) the schematics of the FeN₂ crystal structure with blue color referring to N atoms and red color referring to Fe atoms, (e) the comparison of inverse FFT pattern and projected view of the FeN₂ crystal structure, and (f) simulated diffraction patterns.

5.4 Conclusions

Iron and SS316L become saturated by $5E17$ N/cm², meaning increasing dose does not change their nitrogen profiles. It should be noted that the depth of the nitrogen into

iron and steel, approximately 190 nm for both, extends well beyond that predicted by SRIM, shown in Fig. 5.9. This discrepancy could possibly be attributed to several factors including accelerated diffusion due to induced vacancies by the incident beam, increased diffusion due to beam heating, and/or inaccuracies in the assumed densities [41].

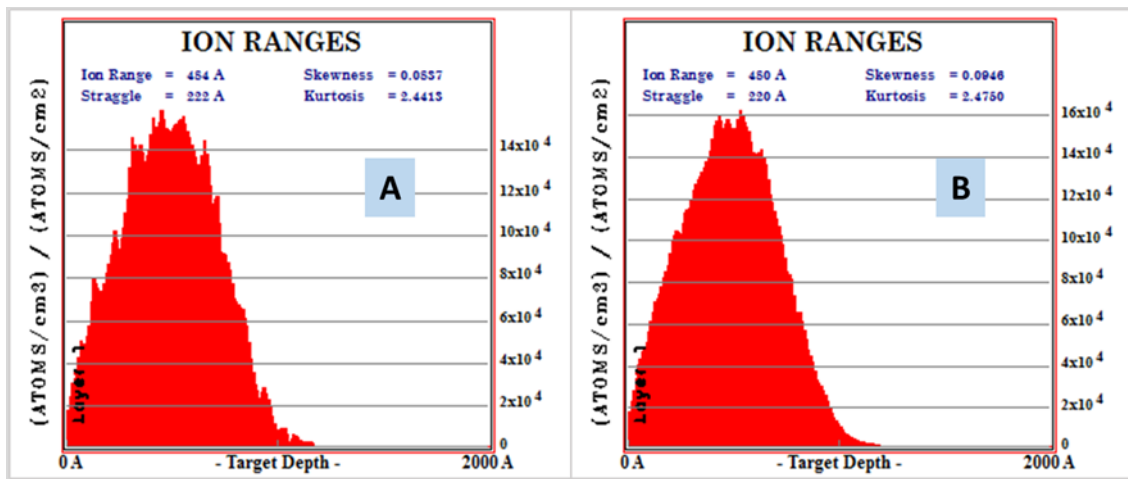


Figure 5.9: SRIM calculations of ion ranges in A) iron and B) SS316L [42].

As nitrogen is introduced into the material matrix, it begins occupying interstitial sites. As the dose is increased in the samples, the possible nitrides that can be formed change. Previous studies by Rauschenbach have shown that the first nitride phase to appear is γ -austenite, as the dose is further increased, α' -martensite appears followed by, α'' -Fe₁₆N₂, γ' -Fe₄N and finally ϵ -Fe₃N. The new nitrides formed as dose increases are the main reason for hardness changes in the room temperature irradiations [42, 43].

The results for the iron dose studies are not in agreement with previous studies. Previous research, including that by Fujihana shown in Fig. 5.10, shows that the hardness

in iron follows a similar trend to SS316L, getting harder to $1\text{E}17\text{ N/cm}^2$ but decreasing by $5\text{E}17\text{ N/cm}^2$. This discrepancy could be of surface quality (i.e. no electropolishing) or more likely surface contamination [39].

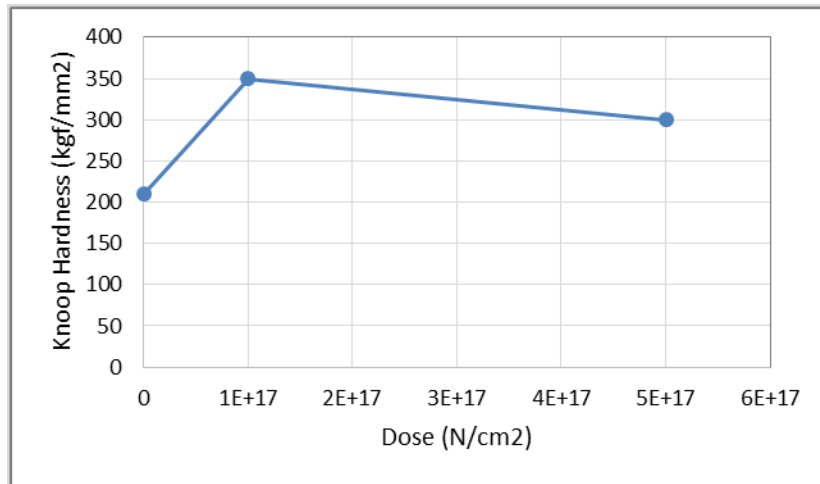


Figure 5.10: Hardness results based on studies by Fujihana [39].

The characterization on the saturated iron sample indicates the presence of Fe_3N and FeN_2 . From previous studies on nitriding it is expected that the Fe_3N phase would be present. However, the presence of the FeN_2 in nitrided materials has not previously been documented.

In the temperature studies it was found that for iron, significant amounts of nitrogen are lost by 300°C . This is in agreement with Rauschenbauch and du Marchie, whose augmented phase diagram can be seen in Fig. 5.11, since they found just above 200°C , γ , α' , and α'' become unstable [43, 44]. The stark increase in hardness at 100°C can be attributed to the change of the α'' - Fe_{16}N_2 phase to the γ' - Fe_4N which occurs around

100°C. Above 300°C, the γ' phase becomes unstable and begins to decrease and is completely gone by 500°C as shown in Fig. 5.4 by the decrease in nitrogen between 300°C and 500°C [45, 46].

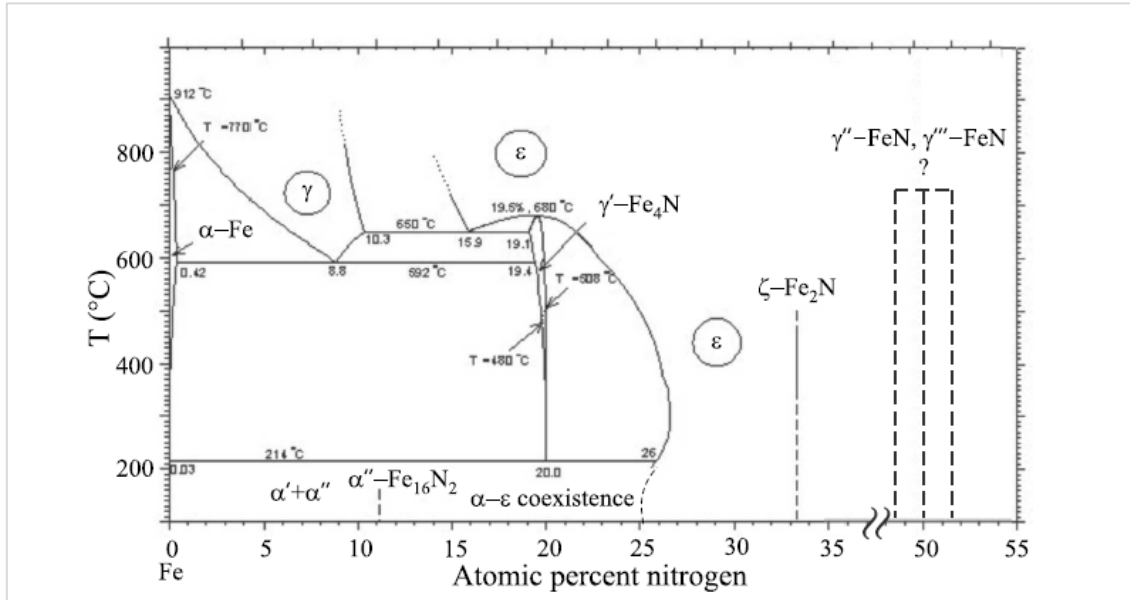


Figure 5.11: Fe-N phase diagram based on findings by du Marchie with augmented γ'' -FeN and γ''' -FeN phases [45].

Since iron is the base material for the SS316L, similar iron phases are likely formed as the dose is increased. However, the alloying elements (C, Cr, Mn, Ni, and Si) have the potential to make many more nitrides that behave differently under annealing as seen in how very little nitrogen is lost between 100°C and 300°C, and how the hardness drastically increases between these temperatures.

For both iron and SS316L a significant increase in hardness can be made through a combination of irradiation and annealing. Iron shows a maximum increase of 1.6 times

the initial hardness, and SS316L shows a maximum increase of 1.5 times. However, the high mobility of the nitrogen in iron alloys at higher temperatures (above 300°C) makes it unlikely that ion nitrided steels would be well suited for reactor conditions. Other nitriding methods create deeper nitride case depths that can withstand higher temperatures for a longer period of time, but it is still unknown if that would be enough to be useful as fuel cladding.

6. ZIRCONIUM AND ZIRCALOY-4

In this section the study of the dose dependence and temperature effects on zirconium and zircaloy-4 are reviewed. The experiment parameters and setup are discussed in detail in section 4.

6.1 Dose Dependence Results

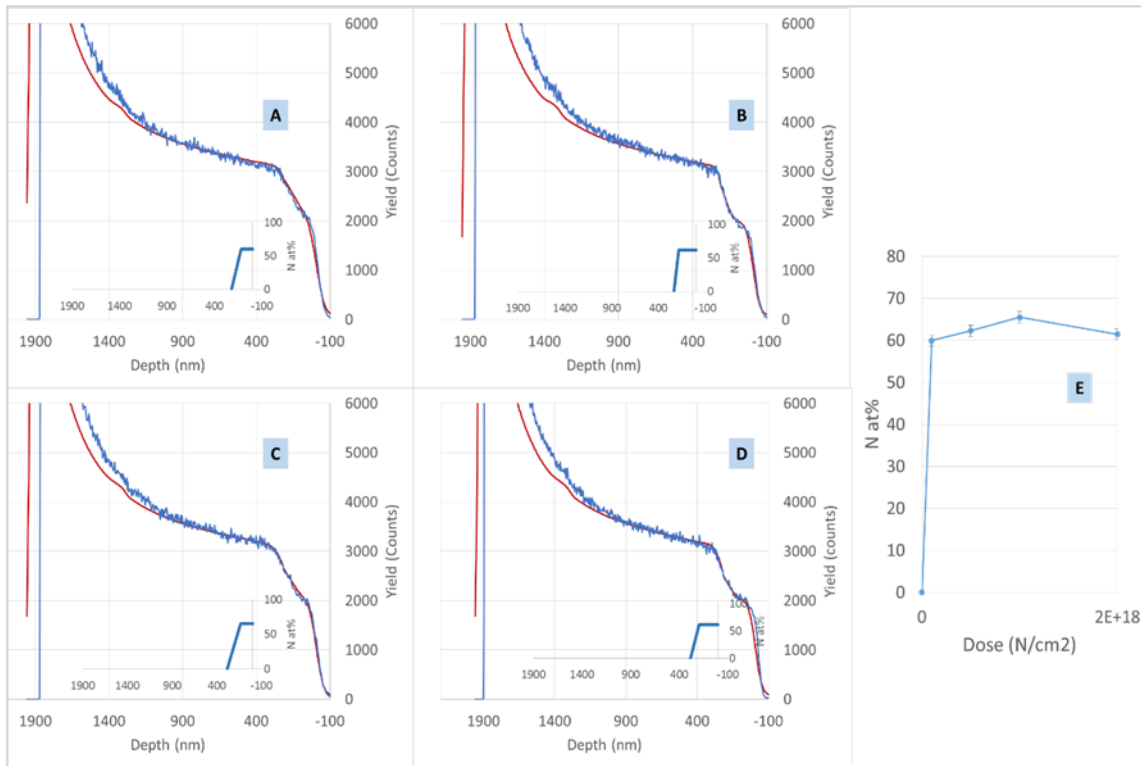


Figure 6.1: RBS spectra and associated nitrogen profiles of pure zirconium irradiated to A) 1E17 N/cm², B) 5E17 N/cm², C) 1E18 N/cm², D) 2E18 N/cm² and E) the concentrations plotted for each dose.

As shown in Fig. 6.1, zirconium reaches its maximum nitrogen concentration by $5E17$ N/cm². However, the nitrogen profile continues to change as the nitrogen diffuses further back into the sample. The final saturation profile is reached by $1E18$ N/cm². The results for zircaloy-4 are in Fig. 6.2 and are similar to zirconium, reaching a saturation profile by $1E18$ N/cm². Differences in the front tail region can be attributed to high background noise during acquisition.

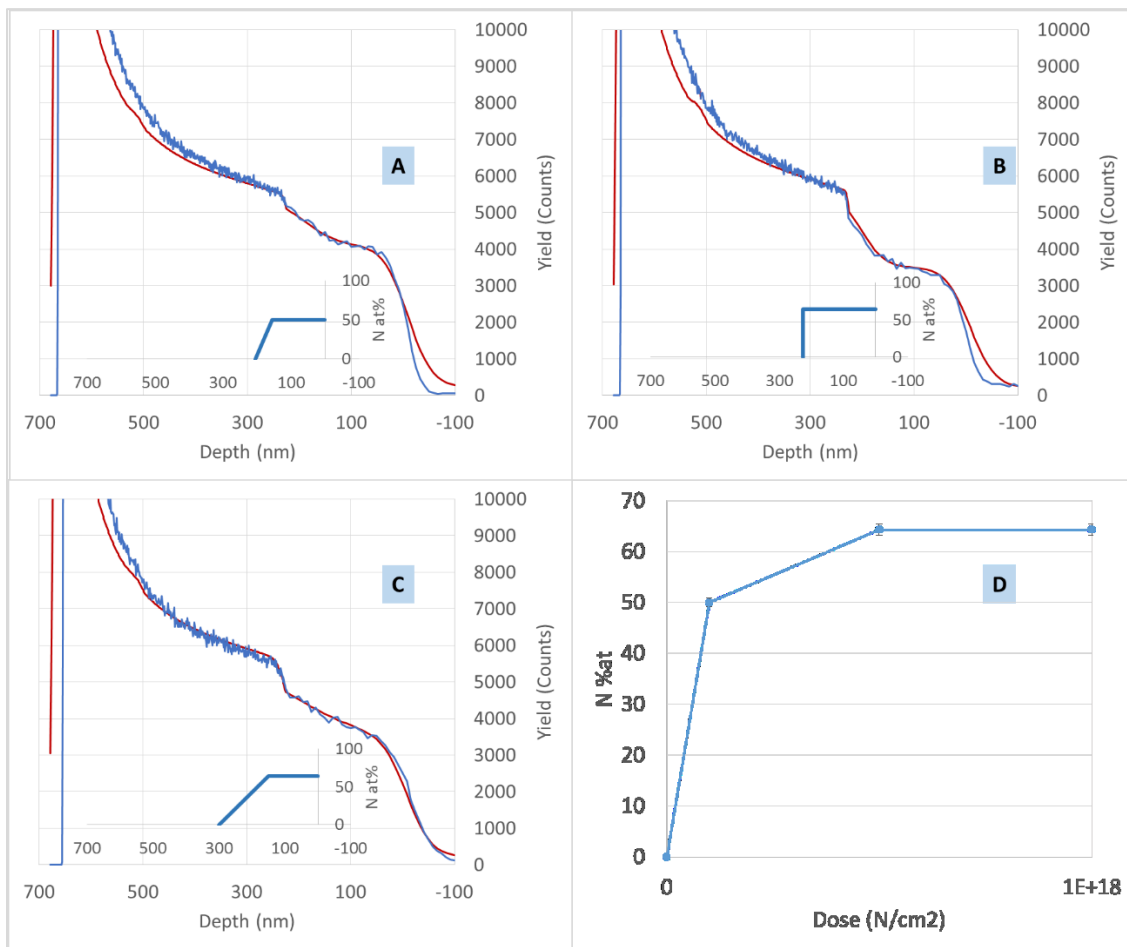


Figure 6.2: RBS spectra and associated nitrogen profiles of zircaloy-4 irradiated to A) $1E17$ N/cm², B) $5E17$ N/cm², C) $1E18$ N/cm², D) $2E18$ N/cm² and E) the concentrations plotted for each dose.

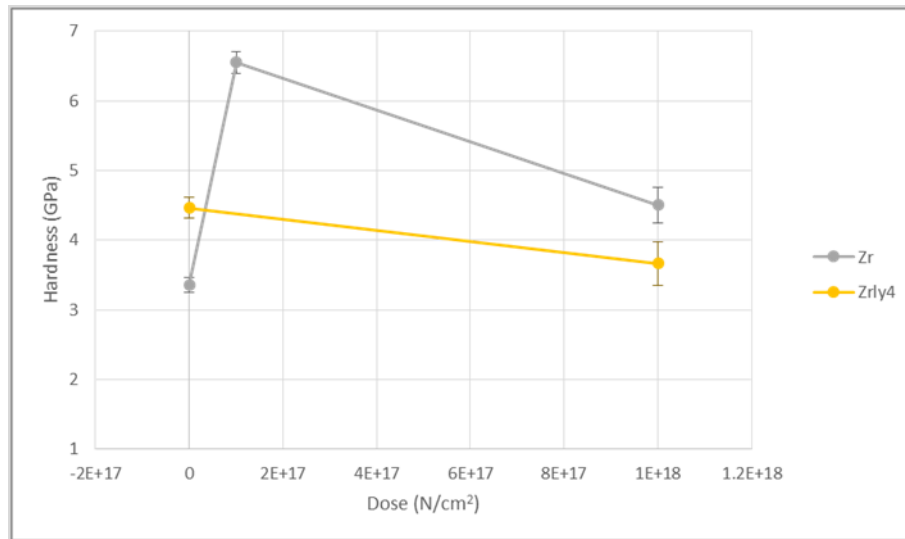


Figure 6.3: Hardness of zirconium and at increasing doses.

The hardness data, in Fig. 6.3, shows similar trends to what was found for the iron and SS316L samples. Zirconium drastically increases in hardness to 1E17 N/cm², but decreases in hardness by 1E18 N/cm². Only two points were able to be acquired for the zircaloy-4, so it is not possible to tell if the zircaloy-4 increased in hardness at any dose before reaching saturation. However, it is clear that when the zircaloy-4 is saturated, the hardness decreases.

6.2 Temperature Stability Results

The temperature tests on zirconium, displayed in Fig. 6.4, show that the nitrogen concentration remains constant until at least 500°C. By 600°C, nitrogen is lost mainly through diffusion further into the sample and the remainder lost through diffusion out of the sample. This indicates that the nitrides formed are stable until at least 500°C, but become unstable by 600°C. Still, by 600°C, most of the nitrogen is still present.

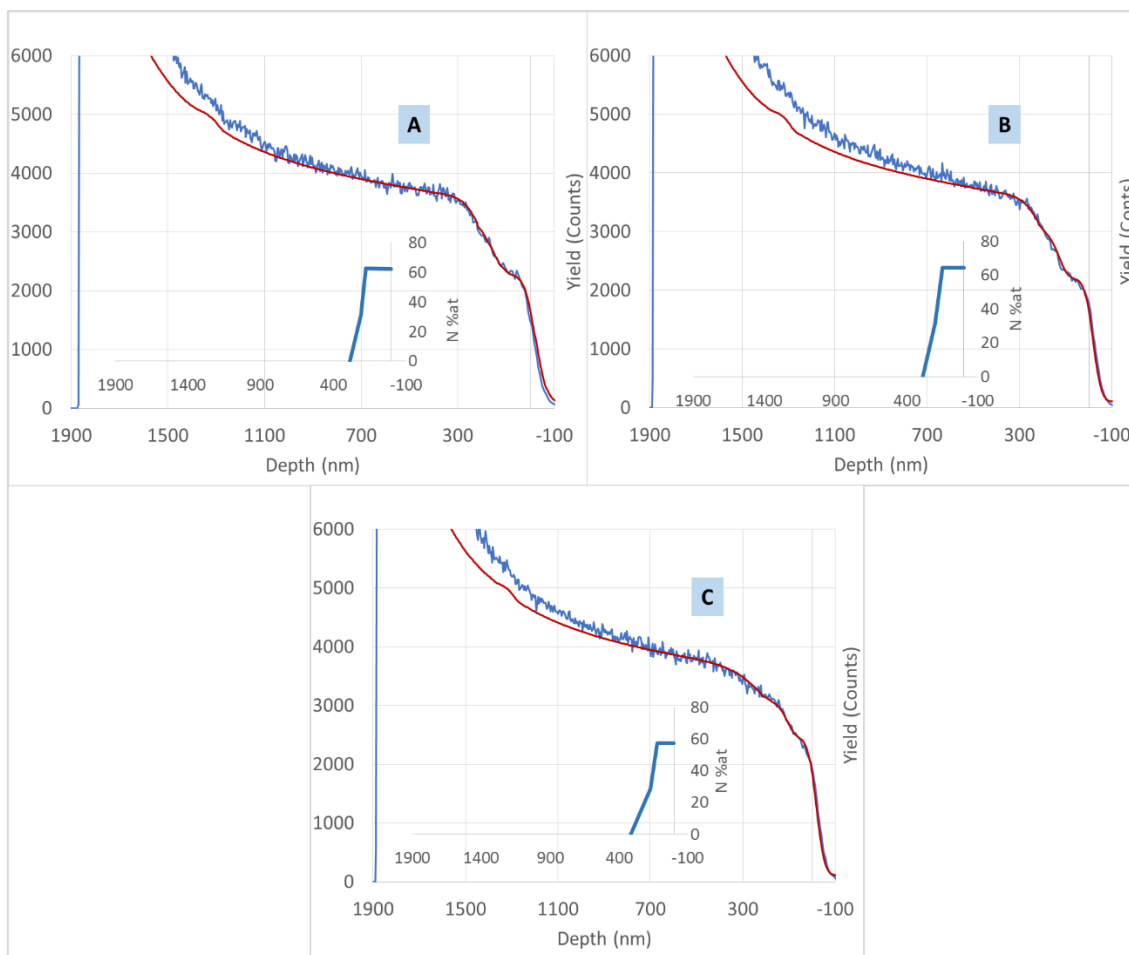


Figure 6.4: RBS spectrum of saturated zirconium post annealed at A) room temperature, B) 500°C, and C) 600°C.

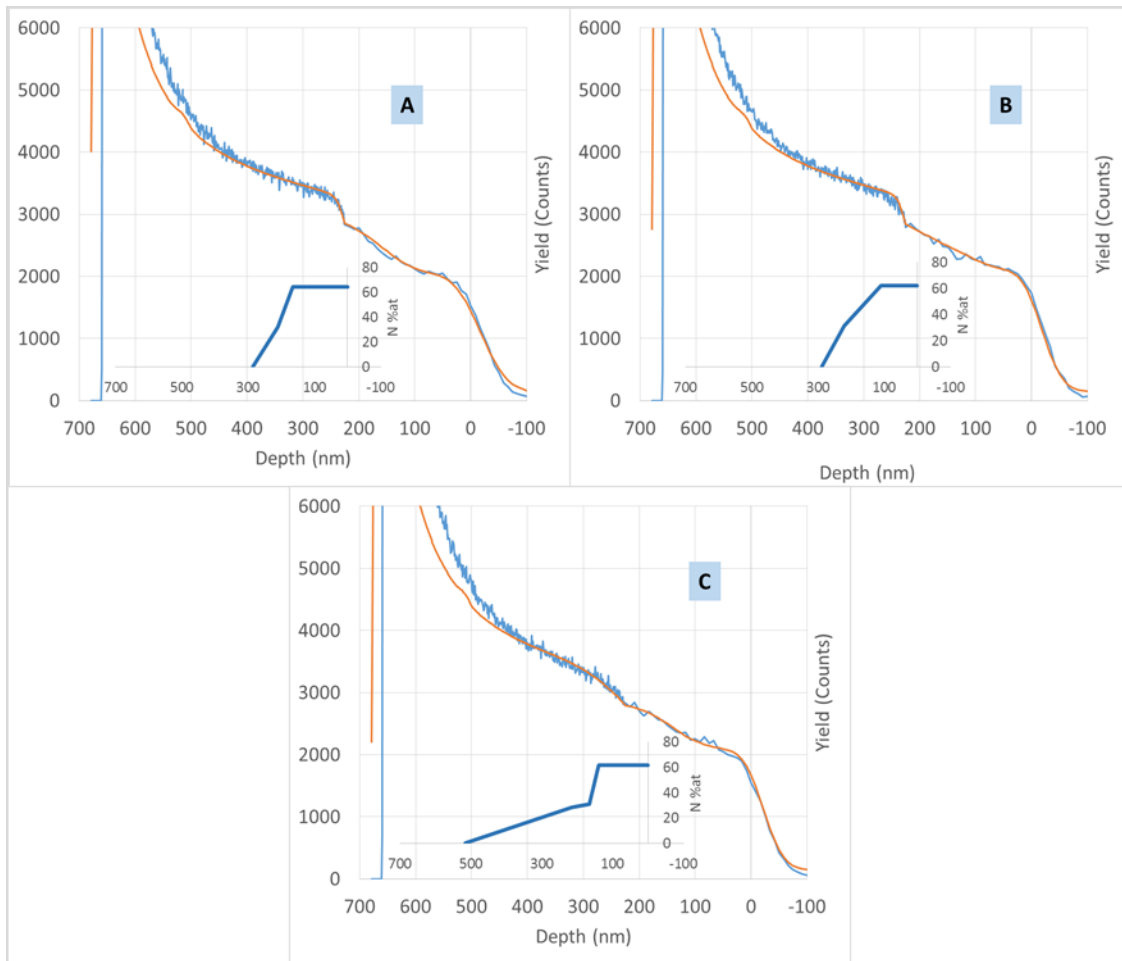


Figure 6.5: RBS spectrum of saturated zircaloy-4 post annealed at A) room temperature, B) 500°C, and C) 600°C.

Like zirconium, the zircaloy-4 tests in Fig. 6.5, show that the nitrogen concentration remains constant until at least 500°C, By 600°C, some nitrogen is lost as it diffuses further into the sample and out of the sample. This indicates that all the nitrides formed are stable until at least 500°C, but some become unstable by 600°C.

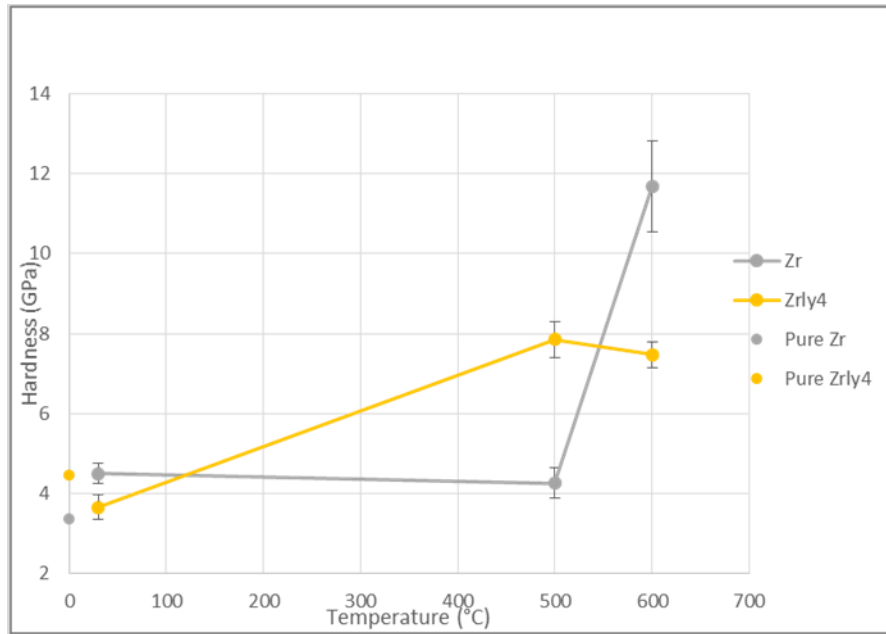


Figure 6.6: Hardness of saturated zirconium and at increasing temperatures.

Hardness tests for the zirconium, shown in Fig. 6.6, indicate that the hardness of both zirconium and zircaloy-4 can greatly be enhanced by a combination of nitrogen implantation and annealing. The zirconium hardness barely changes between room temperature and 500°C, but increases the most drastically of all the hardness changes in this study, by 600°C. Annealing the zircaloy-4 increases the hardness at 500°C and remains almost constant to 600°C.

6.3 Conclusions

Again it should be noted that like the iron and SS316L, the zirconium and zircaloy-4 is well beyond the SRIM predicated range shown in Fig. 6.7. This could be due to

increased diffusion from the induced defects, beam heating, and/or inaccuracies in density assumptions.

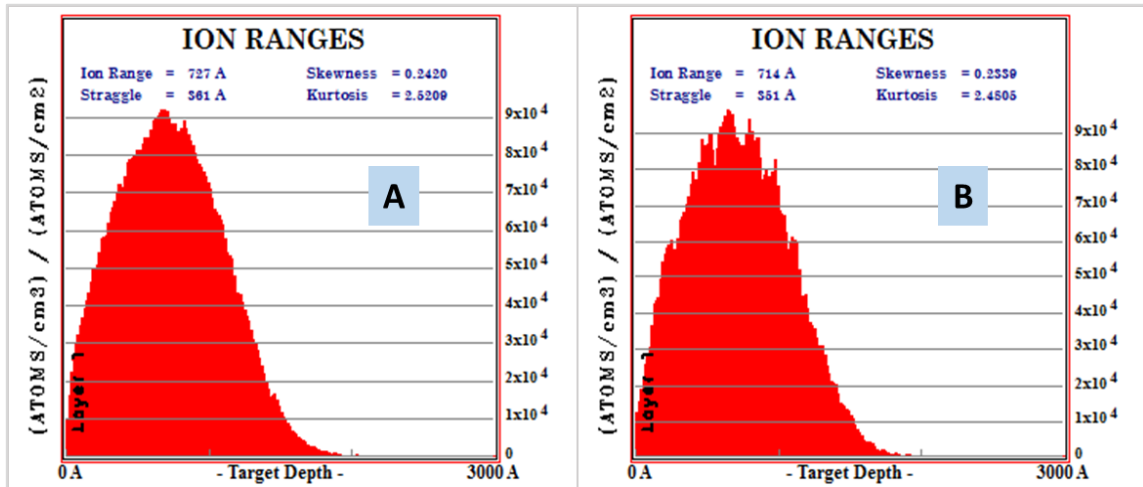


Figure 6.7: Ion ranges of A) zirconium and B) zircaloy-4 calculated by SRIM [42].

The dose dependency tests show that zirconium and zircaloy-4 reach their maximum concentrations at $5E17$ N/cm² and their final saturation profiles at $1E18$ N/cm². As seen from the phase diagram in Fig. 6.8, as nitrogen is implanted into these samples, the zirconium changes phases, and then ZrN is formed. Zircaloy-4 in addition to zirconium, contains tin and trace amounts of iron and chromium. These elements may contribute to the nitrides formed in zircaloy-4.

The hardness test for the dose dependencies shows that there is a peak fluence for which at room temperature a maximum hardness of zirconium can be reached. For zircaloy-4, saturating the sample with nitrogen decreases the hardness at room temperature.

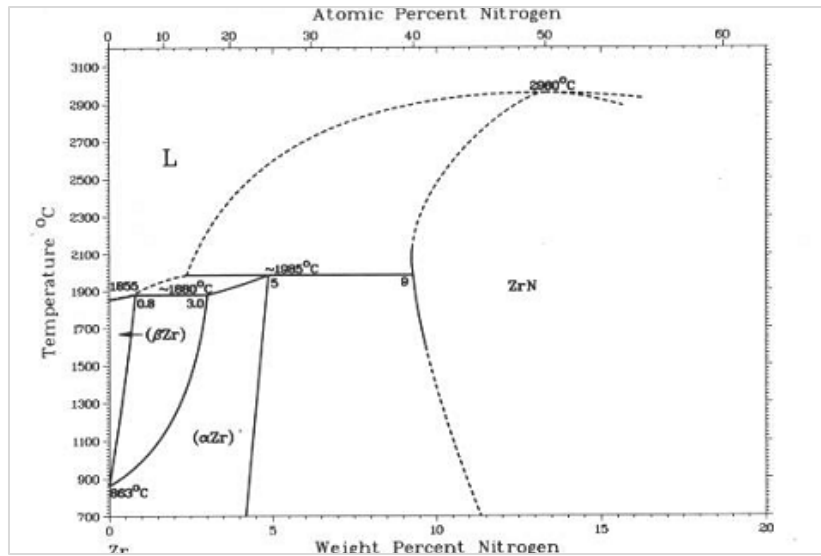


Figure 6.8: Nitrogen-zirconium phase diagram [47].

For the temperature stability tests, it is clear that the ZrN formed is only metastable as it begins to decompose by 600°C, indicated by the drop in nitrogen in the samples. The phase diagram, Fig. 6.8, indicates that ZrN is formed at room temperature and remains in the ZrN phase up to 600°C [47].

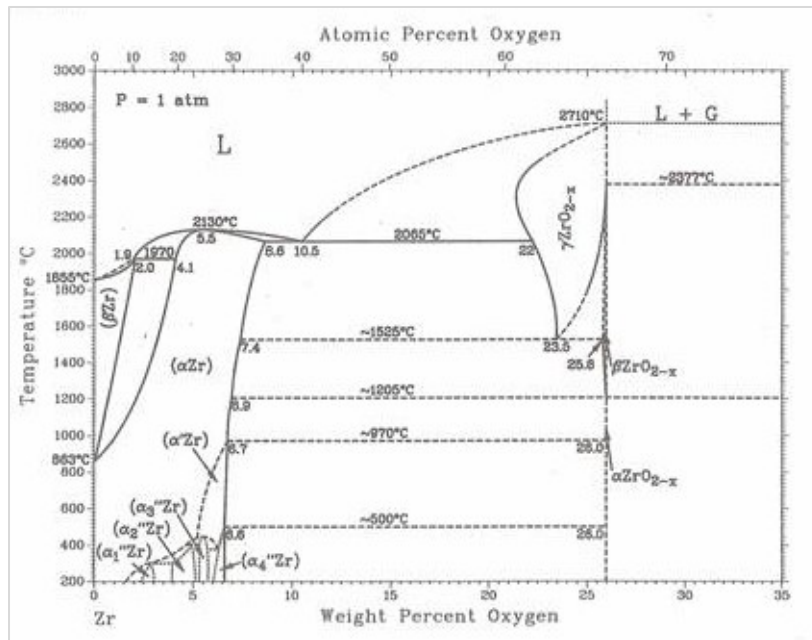


Figure 6.9: Oxygen-zirconium phase diagram [47].

The hardness test show that between room temperature and 500°C, there is little change in hardness for zirconium. For zircaloy-4 however, there is a dramatic increase in hardness most likely as a result of the alloying elements' nitrides. According to the phase diagram, at 600°C, since zirconium does not undergo a phase change, it would be expected that the hardness value would not change [48]. However, zirconium has a massive jump in hardness possibly due to contamination. As seen in Fig. 6.9, zirconium oxides undergo a phase transition at temperatures over 500°C therefore oxygen maybe the contaminant. Zircaloy-4 however, remains at a fairly steady hardness between 500°C and 600°C which is as expected.

Studies by Khan show that other nitrides besides ZrN can be produced during nitriding such as Zr₂N. This means if other phases are present when the dose and

temperature is increased, they could be the causes of concentration and hardness changes in zirconium and zircaloy-4 [47].

Zirconium nitrides formed by ion nitriding appear to be stable at temperatures up to twice as high as iron. This indicates that zirconium nitrides could be stable at temperatures expected of fuel cladding in a reactor.

7. SUMMARY

The fuel cladding in a nuclear reactor contains the majority of the radioactive fission products. Because of this, the cladding is an important safety barrier and maintaining its integrity is vital to the safety and reliability of reactor operation. The events of Fukushima have shown that improvements need to be made to fuel cladding to ensure safety during severe accidents.

One method to potentially improve fuel cladding is through nitriding. The nitriding process works by introducing nitrogen atoms into the surface of a material through implantation or diffusion. The nitrogen forms a nitride layer in the near surface region of the material which can enhance material properties including hardness, wear resistance and corrosion resistance. There are a variety of nitriding processes including ion, plasma, gas, and salt bath.

In this paper, studies were done with ion nitriding experiments to examine the dose dependence and temperature stability of the nitride layer in fuel cladding materials. A particle accelerator was used to implant nitrogen into iron, SS316L, zirconium, and zircaloy-4 materials at different doses. Samples saturated with nitrogen were annealed to various temperatures. Data acquisition was accomplished with RBS, TEM and hardness testing. The data acquired from RBS was analyzed using RUMP software.

The dose dependence test showed that iron and SS316L reach their saturation profiles by a dose of $5E17$ N/cm² and zirconium and zircaloy-4 by $1E18$ N/cm². TEM results from the saturated iron sample indicate the presence of Fe₃N and FeN₂. Previous

studies have shown that the hardness of iron increases to certain dose but past that, increasing the nitrogen content will decrease the hardness. The hardness tests on SS316L and zirconium also show similar trends. The trend on zircaloy-4 is inconclusive due to lack of data.

The temperature stability tests indicate that most iron nitrides are unstable by 300°C. The tests on SS316L indicate that the alloying elements greatly increase the temperature stability of the nitrides compared to pure iron. For zirconium and zircaloy the tests indicate that the nitrides may be stable to temperatures twice as high as that for iron alloys.

Through a combination of nitrogen implantation and annealing the hardness of each of the materials could be significantly improved. The change in hardness of the materials was largely due to the types of nitrides formed in the materials at each concentration and temperature.

Future work needs to be done to further study the temperature stability of the nitrides formed in fuel cladding materials by taking the materials to higher temperatures for longer periods of time. The phases formed at different concentrations and temperatures are not well understood for zirconium and zirconium alloys therefore extensive work should also be done to form a complete Zr-N phase diagram.

REFERENCES

- [1] E.J. Mittemeijer. Fundamentals of nitriding and nitrocarburizing. *ASM Handbook*, 4(A):619-643, 2013.
- [2] D. Pye. Practical nitriding and ferritic nitrocarburizing. *ASM International*, Materials Park, OH, 2003.
- [3] M. Schneider, N. Chatterjee. Introduction to surface hardening of steels. *ASM Handbook*, 4(A):389-398, 2013.
- [4] J. Agren. Diffusion in phases with several components and sublattices. *Journal of Physics and Chemistry of Solids*, 43(5):421-430.
- [5] M. Yang. Nitriding-fundamentals, modeling and process optimization. *Worcester Polytechnic Institute (Ph.D Dissertation)*, Worcester, MA, 2012.
- [6] R. Kubo. Statistical-mechanical theory of irreversible processes. *Journal of Physics Society, Japan*, 12:570-586, 1957.
- [7] A. Biro, Trends of nitriding processes. *Production Processes and Systems*, 6(1):57-66, 2013.
- [8] L. Yuan-hui, L. De-fu, W. Shao-xu. QPQ salt bath nitriding and corrosion resistant. *Trans Tech Publications*, Switzerland, 118:131-136, 2006.
- [9] Dane Buller. Plasma nitride (TiN). 2014. <https://danebuller.wordpress.com/page/2/>
- [10] Services. *Iontech Ltd*. 2012. <http://www.ionitech.net/solutions/services.html>
- [11] Ion plasma/ Ion nitriding (DHIN). *IBC Coatings Technologies, Inc*. 2013. <http://www.ibccoatings.com/ion-plasma-ion-nitriding-dhin>
- [12] ASPN – Active screen plasma nitriding. *ALD Vacuum Technologies*. 2010. <http://web.ald-vt.de/cms/vakuum-technologie/technologien/vacuum-heat-treatment/aspn-active-screen-plasma-nitriding/>
- [13] A. Basu, J. Majumdar, J. Alphonsa, S. Mukherjee, I. Manna. Corrosion resistance improvement of high carbon low alloy steel by plasma nitriding. *Material Letters*, 62(17-18):3117-3120, 2008.

- [14] R. Baracaldo, J. Benito, E. Cabrera, M. Staia. High temperature wear resistance of (TiAl) PVD coating on untreated and gas nitrided AISI H13 steel with different heat treatments. *Wear*, 262(3-4):380-389, 2007.
- [15] C. Azevedo. Selection of fuel cladding material for nuclear fission reactors. *Engineering Failure Analysis*, 18(8):1943-1962, 2011.
- [16] Nuclear fuel fabrication. *World Nuclear Association*, 2016. <http://www.world-nuclear.org/information-library/nuclear-fuel-cycle/conversion-enrichment-and-fabrication/fuel-fabrication.aspx>
- [17] T.R. Allen, R.J.M. Konings, A.T. Motta. Corrosion of Zirconium Alloys. *Comprehensive Nuclear Materials*, 5(3):49-68, 2012.
- [18] R. Hargraves, R. Moir. Liquid fuel nuclear reactors. *American Physical Society*, 2011. <https://www.aps.org/units/fps/newsletters/201101/hargraves.cfm>
- [19] N. Haddar, A. Fissolo, V. Maillot. Thermal fatigue crack networks: a computational study. *International Journal of Solids and Structures*, 42(2):771-788, 2005.
- [20] V. Maillot, A. Fissolo, G. Degallaix, S. Degallaix. Thermal fatigue crack networks parameters and stability: an experimental study. *International Journal of Solids and Structures*, 42(2):759-769, 2005.
- [21] M. Mashayekhi, A. Taghipour, A. Askari, M. Farzin. Continuum damage mechanics application in low-cycle thermal fatigue. *International Journal of Damage Mechanics*, 0:1056789515612532v1-1056789515612532, 2015.
- [22] G. Halford. Low-cycle thermal fatigue. *NASA*. 1986
- [23] L. Tang, S. Ding, Y. Huo. Fretting fatigue analysis on nuclear fuel cladding tubes. *Fudan University*, Shanghai, China, 2013. <http://www.gruppofrattura.it/ocs/index.php/ICF/icf13/paper/viewFile/11260/10639>
- [24] Y. Lee, H. Kim. Fretting wear behavior of a nuclear fuel rod under a simulated primary coolant condition. *Wear*, 301(s 1-2):569-574, 2013.
- [25] Delayed hydride cracking of zirconium alloy fuel cladding. *International Atomic Energy Agency*, IAEA-TECDOC-1649, 2010.
- [26] C. Coleman, V. Grigoriev, V. Inozemtsev, V. Markelov, M. Roth, et.al. Delayed hydride cracking in zircaloy fuel cladding – an IAEA coordinated research programme. *Nuclear Engineering and Technology*, 41(2):171-178, 2009.

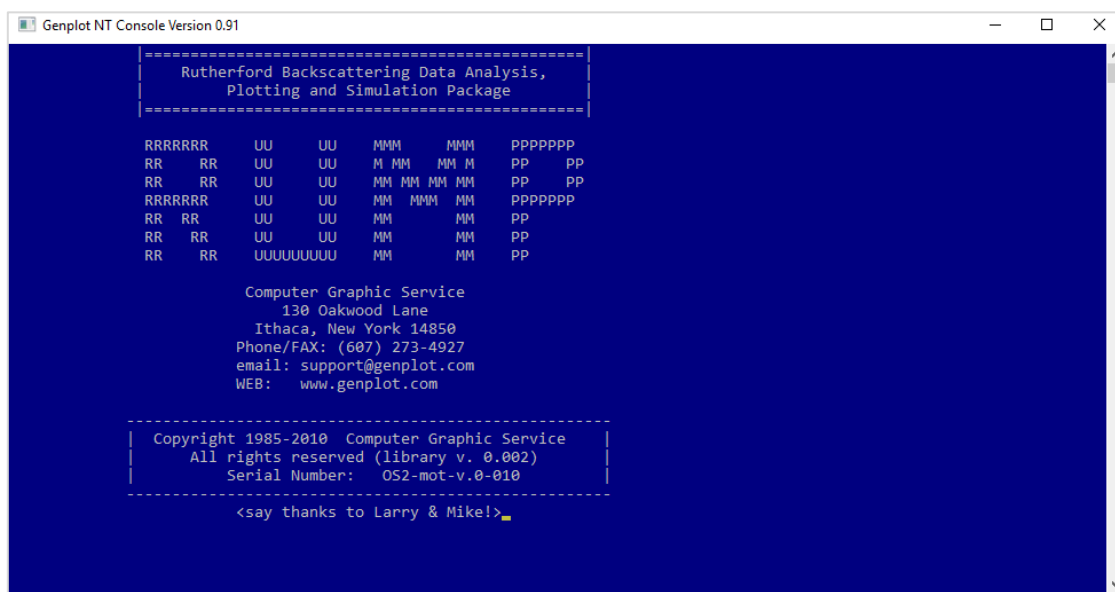
- [27] T. Spence. Corrosion resistant zirconium castings. *NACE International*, 2001.
http://foundry.flowserve.com/materials/article_corrosion.stm
- [28] K. Chan. An assessment of delayed hydride cracking in zirconium alloy cladding tubes under stress transients. *International Materials Reviews*, 58(6):349-373, 2013.
- [29] A. Fraker. Corrosion of zircaloy spent fuel cladding in a repository. *U.S. Department of Commerce*, 1989.
- [30] A. Abe, C. Giovedi, D. Gomes and A. Silva. Revisiting stainless steel as PWR fuel rod cladding after Fukushima Daiichi accident. *Journal of Energy and Power Engineering*, 8:973-980, 2014.
- [31] J. Yanez, M. Kuznetsov, A. Iglesias. An analysis of the hydrogen explosion in the Fukushima-Daiichi Accident. *International Journal of Hydrogen Energy*, 40(25):8261-8280, 2015
- [32] I. Jain, G. Agarwal. Ion beam induced surface and interface engineering. *Surface Science Reports*, 66(3-4):77-172, 2011.
- [33] G. Lopez, Understanding and controlling native defect assisted diffusion of acceptors in silicon: a theoretical study. *Universita Degli Studi Cagliari (Ph.D Dissertation)*, Cagliari, Italy, 2004.
- [34] The Geiger-Marsden experiment. *The Physics Teacher*, 2015.
<http://apphysics.david-s.org/geiger-marsden-experiment/>
- [35] The gold foil experiment (Ernest Rutherford). *Purdue*, 2005.
<http://chemed.chem.purdue.edu/genchem/history/gold.html>
- [36] RBS theory. *Evans Analytical Group*, 2013. <http://www.eag.com/mc/rbs-theory.html>
- [37] M. Mayer. Rutherford backscattering spectrometry. *EURATOM Association*, 2003.
http://users.ictp.it/~pub_off/lectures/lms022/Mayer_1/Mayer_1.pdf
- [38] L. Doolittle, M. Thompson, R. Cochran. RUMP. *Cornell*, 2013.
<http://www.genplot.com/doc/rump.htm>
- [39] T. Fujihana, Y. Okabe, M. Iwaki. Microstructure and mechanical properties of high dose nitrogen-implanted iron, chromium and titanium sheets. *Material Science and Engineering: A*, 115: 291-295, 1989.

- [40] L. Price, A study of the crystallization and amorphization mechanisms of metallic glasses under ion bombardment. *Texas A&M University (Ph.D Dissertation)*, College Station, TX, 2016.
- [41] G. Dearnaley. The effects of ion implantation upon the mechanical properties of metals and cemented carbides. *Radiations Effects*, 63(1-4), 1982.
- [42] James F. Ziegler, M.D. Ziegler, and J.P. Biersack. SRIM: Stopping range of ions in matter. 2010. <http://www.srim.org/>
- [43] B. Rauschenback, A. Kolitsch. Formation of compounds by nitrogen ion implantation in iron. *Physica Status Solidi*, 80(1):211-222, 1983.
- [44] B. Rauschenback, A. Kolitsch, K. Hohmuth. Iron nitride phases formed by nitrogen ion implantation and thermal treatment. *Physica Status Solidi*, 80(1):471, 1983.
- [45] E. Du Marchie, D. Boerma, N. Chechenin. Low-temperature extension of the Lehrer diagram and the iron-nitrogen phase diagram. *Metallurgical and Materials Transactions A*, 33(8)2593-2598, 2002.
- [46] D. Borsa. Nitride-based insulating and magnetic thin films and multilayers. *University of Groningen (Ph. D Thesis)*, Groningen, Netherlands, 2004. <http://www.rug.nl/research/portal/files/9805326/thesis.pdf>
- [47] J. Riha, P. Sutta. Zirconium phase transformations measured by “in-situ” X-ray diffraction. *University of West Bohemia*, 2016. <http://www.xray.cz/xray/csca/kol2011/abst/riha.htm>
- [48] I. Khan, M. Hassan, R. Ahmad, A. Qayyum, G. Murtaza, et al. Nitridation of zirconium using energetic ions from plasma focus device. *Thin Solid Films*, 516(23):8255-8263, 2008.

APPENDIX A

The following steps demonstrate how to import a data file, acquired from RBS, into RUMP, and how to analyze it with RUMP software. RUMP and GENPLOT are required to run the simulations.

1: OPEN RUMP



```
Genplot NT Console Version 0.91

-----
Rutherford Backscattering Data Analysis,
Plotting and Simulation Package
-----

RRRRRRR   UU   UU   MMM   MMM   PPPPPPP
RR  RR   UU   UU   M MM   MM M   PP  PP
RR  RR   UU   UU   MM MM MM MM   PP  PP
RRRRRRR   UU   UU   MM  MMM  MM   PPPPPPP
RR  RR   UU   UU   MM   MM   MM   PP
RR  RR   UU   UU   MM   MM   MM   PP
RR  RR   UU   UU   MM   MM   MM   PP
RR  RR   UUUUUUUU  MM   MM   MM   PP

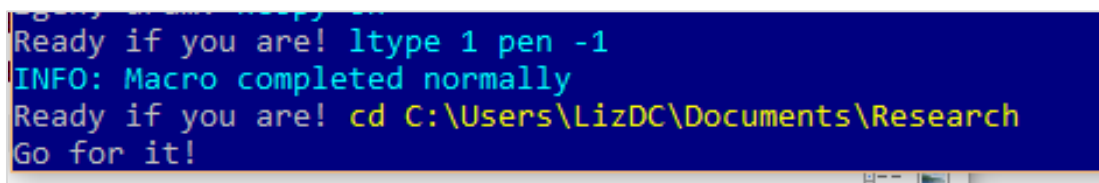
Computer Graphic Service
130 Oakwood Lane
Ithaca, New York 14850
Phone/FAX: (607) 273-4927
email: support@genplot.com
WEB: www.genplot.com

-----
Copyright 1985-2010 Computer Graphic Service
All rights reserved (library v. 0.002)
Serial Number: 052-mot-v.0-010
-----

<say thanks to Larry & Mikel!>
```

Figure A.1: Picture of RUMP software opening display.

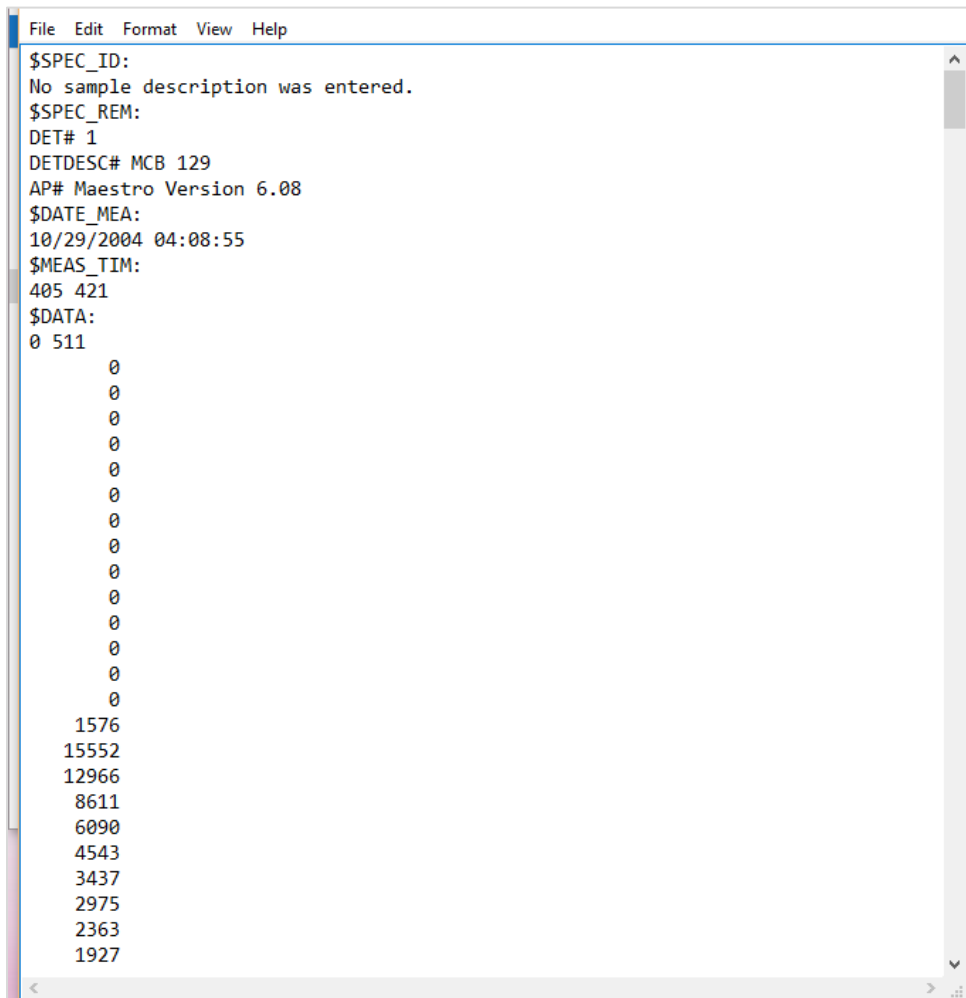
2: CHANGE TO DESIRED DIRECTORY



```
Ready if you are! ltype 1 pen -1
INFO: Macro completed normally
Ready if you are! cd C:\Users\LizDC\Documents\Research
Go for it!
```

Figure A.2: Picture of directory change input in RUMP.

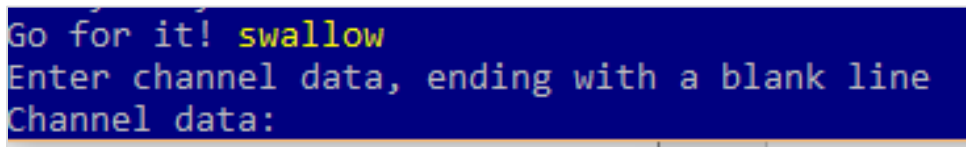
3: OPEN DATA FILE AND COPY DATA



```
File Edit Format View Help
$SPEC_ID:
No sample description was entered.
$SPEC_REM:
DET# 1
DETDESC# MCB 129
AP# Maestro Version 6.08
$DATE_MEA:
10/29/2004 04:08:55
$MEAS_TIM:
405 421
$DATA:
0 511
    0
    0
    0
    0
    0
    0
    0
    0
    0
    0
    0
    0
    0
    0
    0
    1576
    15552
    12966
    8611
    6090
    4543
    3437
    2975
    2363
    1927
```

Figure A.3: Picture of data from a typical RBS text file.

4: LOAD DATA IN RUMP USING SWALLOW COMMAND



```
Go for it! swallow
Enter channel data, ending with a blank line
Channel data:
```

Figure A.4: Picture of swallow command used in RUMP.

5: PLOT DATA, ENSURE DATA IS CORRECT

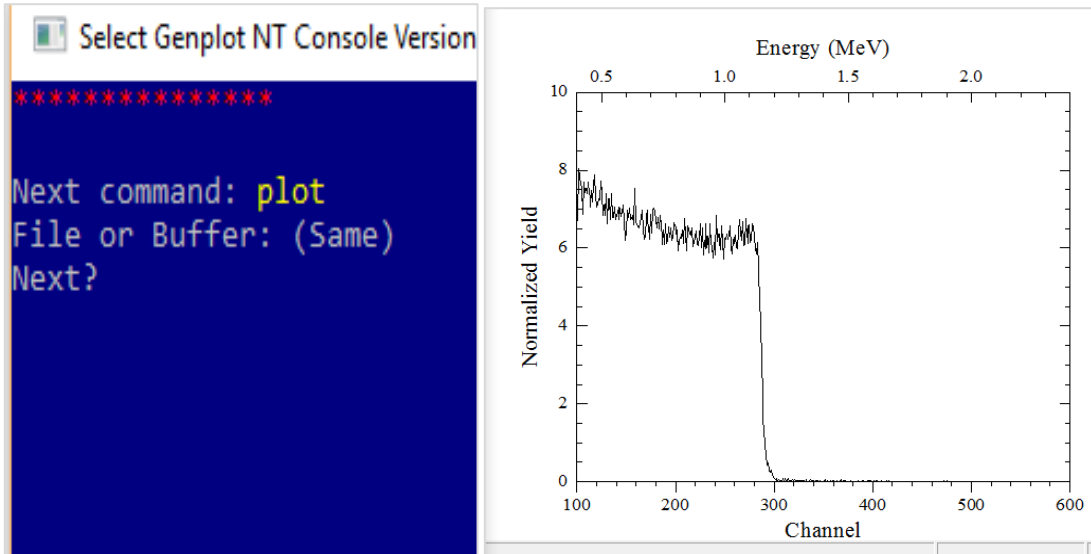


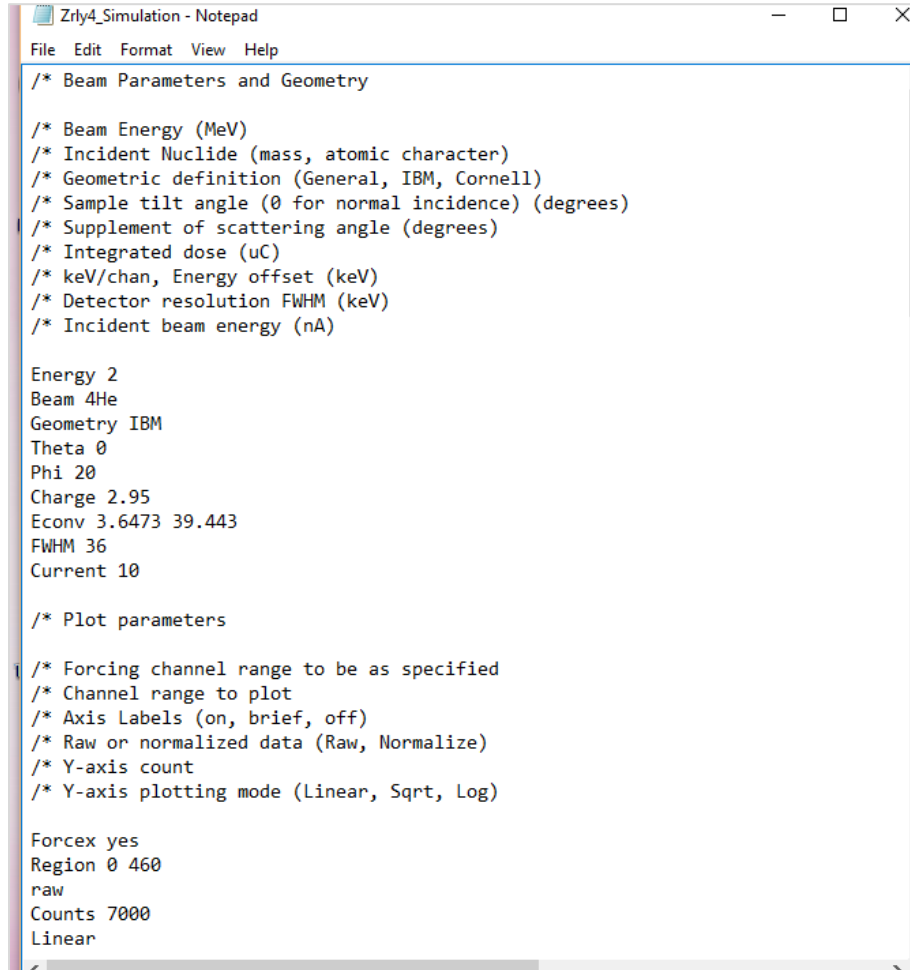
Figure A.5: Picture of plot command used in RUMP (left) and associated generated graph of data (right).

6: SAVE DATA AS .RBS FILE USING WRITE COMMAND

The figure is a screenshot of a terminal window titled "Genplot NT Console Version 0.91". The text in the terminal is as follows: "File or Buffer: (Same)", "Next? write", "Filename to write (abort): silicon.rbs", "WARNING: The actual numerical counts in C:\Users\LizDC\Documents\Research\silicon.rbs has been changed (smoothing or otherwise). Saving modified experimental data is generally a bad idea. Proceed with caution!", "*** Do you still want to proceed and write the file (NO)? y", and "Beam me up Scottie! _".

Figure A.6: Picture of write command used in RUMP.

7: MAKE A .TXT FILE USING PARAMATERS CALCULATED FROM
STANDARD SAMPLES AND INPUT FILE



```
File Edit Format View Help
/* Beam Parameters and Geometry
/* Beam Energy (MeV)
/* Incident Nuclide (mass, atomic character)
/* Geometric definition (General, IBM, Cornell)
/* Sample tilt angle (0 for normal incidence) (degrees)
/* Supplement of scattering angle (degrees)
/* Integrated dose (uC)
/* keV/chan, Energy offset (keV)
/* Detector resolution FWHM (keV)
/* Incident beam energy (nA)

Energy 2
Beam 4He
Geometry IBM
Theta 0
Phi 20
Charge 2.95
Econv 3.6473 39.443
FWHM 36
Current 10

/* Plot parameters
/* Forcing channel range to be as specified
/* Channel range to plot
/* Axis Labels (on, brief, off)
/* Raw or normalized data (Raw, Normalize)
/* Y-axis count
/* Y-axis plotting mode (Linear, Sqrt, Log)

Forcex yes
Region 0 460
raw
Counts 7000
Linear
```

Figure A.7: Picture of input text file for RUMP.

8: CREATE LAYERS AND PLOT SIMULATION AGAINST DATA

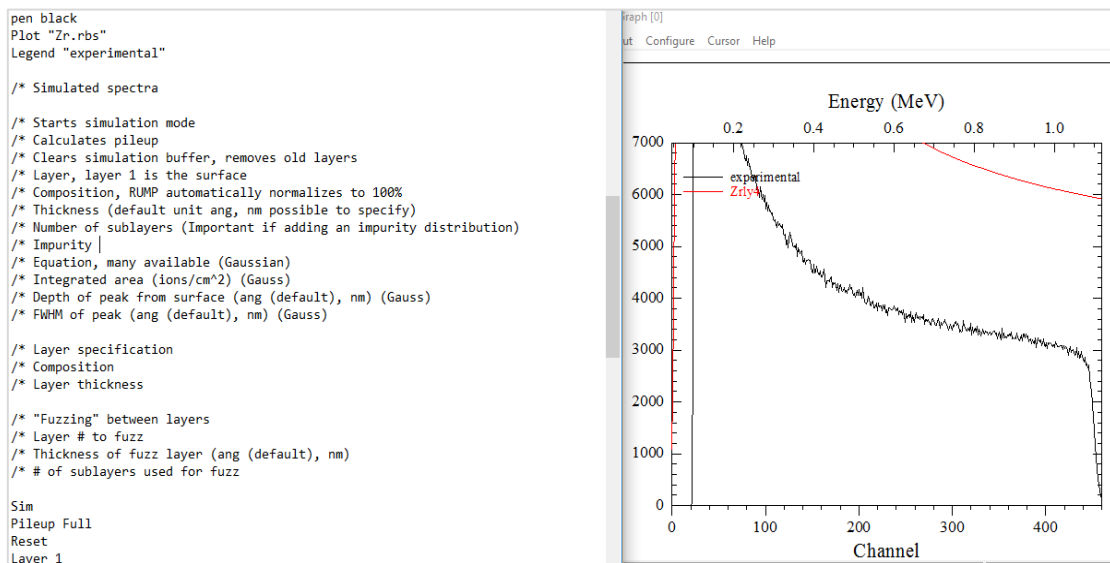


Figure A.8: Picture of input text file and associated RUMP plot.

9: ADJUST LAYER THICKNESS AND COMPOSITION TO MATCH DATA

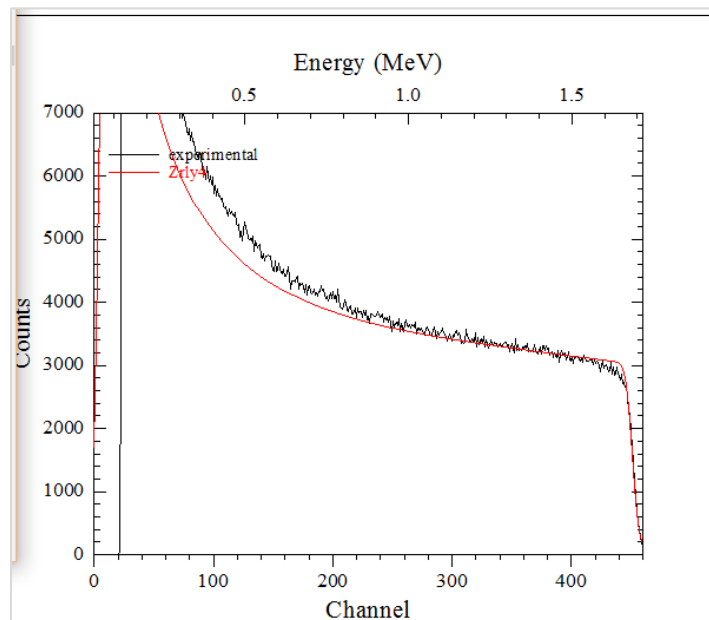


Figure A.9: Picture of simulation and data plots generated by RUMP.

10: SAVE DATA AS .TXT FILE

```
/* Tells RUMP to look at a specific buffer (buffer 0 is where the simulation dat
/* Writes data to a text file, which then can be copied to your preferred plottin
/* File name of choice
Pointat 0
WRASCII
"Sim_Zr.txt"
```

Figure A.10: Picture of commands used to save data file.